Petroleum Science 23 (2026) 998–1013

Contents lists available at ScienceDirect

Petroleum Science

journal homepage: www.keaipublishing.com/en/journals/petroleum-science

Original Paper

Changes in the effective absolute permeability of hydrate-bearing sands during isotropic loading and unloading

Hui-Long Ma [a], Xiu-Li Feng [a], Le-Le Liu [b,c,*], An Zhang [b], Dong Wang [b]

[a] College of Marine Geosciences, Ocean University of China, Qingdao, 266100, Shandong, China
[b] Shandong Engineering Research Center of Marine Exploration and Conservation, Ocean University of China, Qingdao, 266100, Shandong, China
[c] Laboratory for Marine Mineral Resources, Qingdao Marine Science and Technology Center, Qingdao, 266237, Shandong, China

ARTICLE INFO

Article history:
Received 10 July 2025
Received in revised form
2 September 2025
Accepted 13 October 2025
Available online 16 October 2025

Edited by Min Li

Keywords:
Gas hydrate
Depressurization
Compression and swelling
Permeability stress sensitivity
Mean effective stress

ABSTRACT

The effective stress of marine sediments frequently shifts owing to natural or anthropogenic factors, and a broad spectrum of processes fundamentally require accounting for sediment responses to such changes. Marine sediments hosting natural gas hydrates have been regarded as a prospective energy reservoir, and depressurization-driven production efficiency hinges largely on the effective absolute permeability of hydrate-bearing strata. Yet, how this permeability evolves during depressurization remains unresolved, and whether pore-hosted hydrates impede or enhance it remains ambiguous. This study probes the permeability response of hydrate-bearing sands to cyclic loading through isotropic compression/swelling and water flow tests. Results reveal that methane hydrate presence curbs the void-ratio decline yet amplifies the effective-void-ratio reduction during isotropic loading. The effective absolute permeability of hydrate-bearing sands declines with rising hydrate saturation and increasing mean effective stress, and permeability stress sensitivity intensifies at higher hydrate saturations and lower mean effective stresses. The introduced model accurately predicts void-ratio changes during isotropic loading and unloading. Coefficients for strengthening, normal filling, and enhanced filling effects are introduced and quantified to disentangle the positive and negative influences of methane hydrate, with the negative filling effect exceeding the positive strengthening effect by one order of magnitude for quartz sands.

1. Introduction

Changes in the effective stress of marine sediments are frequently encountered across diverse processes. Examples encompass the marine sedimentation process wherein the vertical effective stress incrementally escalates with progressive burial depth (Sawyer and DeVore, 2015), the internal wave propagation process wherein bed-stress amplification manifests (Zulberti et al., 2020), the deep-sea hard minerals extraction process wherein seabed sediments are subjected to loading by mining vehicles (Zhang et al., 2025a), and the deliberately induced pore fluid injection for offshore carbon dioxide sequestration (Cao et al., 2025; Zhao et al., 2024) alongside pore fluid withdraw for natural gas hydrate exploitation (Cai et al., 2020; Kim et al., 2018). Accounting for responses of marine sediments to alterations in effective stress is imperative for evaluating sedimentation-governed seabed instability (Stoecklin et al., 2017), optimizing the engineering of deep-sea mining vehicles (Sun et al., 2022), and appraising the carbon sequestration efficiency together with the economic viability of hydrate production (Khan et al., 2024; Wan et al., 2022).

Natural gas hydrates constitute crystalline solid compounds naturally present within marine sediments along the continental margin (Sloan, 2003), and they have been recognized as a prospective energy resource owing to their extensive occurrence and capacity to concentrate substantial methane volumes (Chong et al., 2016). Methane recovery from natural gas hydrates entails fully coupled thermal-hydraulic-mechanical-chemical processes (Gong et al., 2025), and depressurization presently serves as the favored technique for offshore hydrate production field trials (Li et al., 2018; Yamamoto et al., 2019; Ye et al., 2020). History-

* Corresponding author.
E-mail address: lele.liu@ouc.edu.cn (L.-L. Liu).
Peer review under the responsibility of China University of Petroleum (Beijing).

https://doi.org/10.1016/j.petsci.2025.10.009

matching simulations of these trials (Ouchi et al., 2022; Zhou et al., 2020a) alongside parameter sensitivity analyses (Huang et al., 2016; Liu et al., 2015) reveal that gas recovery efficiency is predominantly governed by the hydraulic characteristics of hydrate-bearing sediments, and a fundamental parameter embodying these characteristics is the saturated water permeability (Zhang et al., 2020), alternatively termed the effective absolute permeability (Li et al., 2025). The effective absolute permeability quantifies the ease with which a single-phase fluid (e.g., water) migrates through marine sediments hosting natural gas hydrates in the absence of any additional pore fluid phase. Upon progressive and complete dissociation of solid hydrates, the effective absolute permeability of hydrate-bearing sediments transitions into the absolute or intrinsic permeability of the corresponding hydrate-free sediments (i.e., the host matrix or the host sediments) (Zhang et al., 2023b). The intrinsic permeability of hydrate-free sediments across varying grain-size distributions typically exhibits power-law growth with void ratio (i.e., the ratio of total pore volume over aggregate grain volume) (Ren and Santamarina, 2018). To capture the response of effective absolute permeability to effective stress variations, it is first necessary to elucidate how the void ratio of host sediments evolves during depressurization, given that effective stress increments can exceed 10 MPa under field conditions (Zhou et al., 2020b).

When subjected to external loading and unloading, pore volume variation of the host sediments is markedly influenced by natural gas hydrates owing to their cementation and pore-filling roles (Tian et al., 2024; Zhao et al., 2025). Once these effects vanish upon hydrate dissociation, volumetric contraction of the host sediments ensues, and the void ratio declines under zero-lateral-strain conditions (Dai et al., 2011; Fang et al., 2022; Lee et al., 2010). This reveals that the solid hydrate sustains a portion of the external load, and this load is subsequently transferred to the sediment skeleton after hydrate dissociation, inducing further contraction (Fang et al., 2022). The stiffening contribution of hydrate to the host sediments has been directly visualized via X-ray computed tomography during triaxial shearing experiments (Lei and Seol, 2020). Prior to shearing in triaxial shear tests, isotropic loading is imposed to probe the compressibility of hydrate-bearing sediments (Nakashima et al., 2021; Xu et al., 2022; Yan et al., 2023; Yang et al., 2023; Zhou et al., 2021). Results demonstrate that the void ratio of hydrate-bearing sediments across varying hydrate saturations scarcely alters during the initial isotropic loading stage, and the corresponding compression curves essentially overlap. As the isotropic load continues to rise, the curves progressively diverge, signifying the onset of structural yielding in hydrate-bearing sediments. The yield stress of hydrate-bearing sediments rises linearly (Yan et al., 2023; Yang et al., 2023) or exponentially (Nakashima et al., 2021; Zhou et al., 2021) with increasing hydrate saturation. No consensus exists among experimental dataset regarding how the compression index of hydrate-bearing sediments varies with hydrate saturation; both inverse correlations (Luo et al., 2020; Nakashima et al., 2021; Xu et al., 2022) and essentially no correlation (Yan et al., 2023; Yang et al., 2023; Zhou et al., 2021) have been documented. Grounded in the critical-state framework for soils, the compression index of hydrate-bearing sediments should remain independent of hydrate saturation (Uchida et al., 2012), a proposition that has been scrutinized through numerical simulations (Zhang et al., 2023a).

Since natural gas hydrates occupy the pore space as solids that constrict and may fully occlude fluid pathways within hydrate-bearing sediments, the effective absolute permeability typically declines with rising hydrate saturation, yet the rate of decline can shift markedly when pore habit and morphology differ (Delli and Grozic, 2014; Kumar et al., 2010; Li et al., 2024; Liu et al., 2020; Zhang et al., 2020, 2025b). The pore habit and morphology of natural gas hydrates in situ are governed by host-sediment grain size and the prevailing effective stress state (Dai et al., 2012). Beyond its indirect influence, the effective stress acts as a primary driver of pore volume evolution, thereby directly modifying the effective absolute permeability of hydrate-bearing sediments (Zhang et al., 2023b). Observations reveal that the effective absolute permeability of hydrate-bearing sediments decreases either linearly (Wang et al., 2021) or exponentially (Xu et al., 2024; Zhang et al., 2022; Zhao et al., 2023) with increasing effective stress. Nonetheless, some experiments indicate that the sensitivity of effective absolute permeability to effective stress (hereafter termed permeability stress sensitivity) diminishes when hydrates occupy the pores (Wang et al., 2021), whereas others demonstrate that such sensitivity intensifies with higher hydrate saturations (Zhang et al., 2022; Zhao et al., 2023). Additionally, Wang et al. (2021) reported that permeability stress sensitivity declines under rising effective stress for marine sediments at hydrate saturations of 0 and 0.41, yet rises for hydrate saturations between 0.26 and 0.38. Conversely, Zhao et al. (2023) observed that permeability stress sensitivity monotonically decreases with increasing effective stress for marine sediments up to a hydrate saturation of 0.3. These conflicting findings unequivocally signal that the evolution of effective absolute permeability in hydrate-bearing sediments under combined variations in effective stress and hydrate saturation (e.g., during depressurization) remains unresolved, largely stemming from insufficient insight into the competing enhancing and impeding roles that natural gas hydrates exert on effective absolute permeability.

This study seeks to uncover the dual impacts of pore-hosted natural gas hydrates and to illuminate the effective absolute permeability of hydrate-bearing sediments exposed to isotropic loading and unloading. Isotropic compression/swelling and water flow experiments are performed on quartz sands both with and without methane hydrate occupancy, and variations in pore volume and effective absolute permeability under distinct conditions are investigated, succeeded by evaluations of permeability stress sensitivity. Subsequently, an analytical void-ratio model is formulated to portray intrinsic pore volume evolution during isotropic compression and swelling. Throughout isotropic compression, the beneficial and detrimental influences of methane hydrate upon effective pore volume and effective absolute permeability are quantified, and understanding of the dual hydrate effects is ultimately refined.

2. Experimental program

2.1. Experimental apparatus, materials, and procedures

Fig. 1 depicts the schematic of the experimental setup (GDS Instruments) employed for isotropic compression and water flow experiments on hydrate-bearing sands. The specimen, 50 mm in diameter and 100 mm in height, is encapsulated by two rubber membranes, each 0.5 mm thick. Silicone oil surrounding the membranes transmits pressure from a syringe pump as confining pressure; the operational range reaches 32 MPa with a precision of 0.1% FRO (Full Range Output). A coiled tube, also filled with silicone oil and circulated through a cooling bath, encircles the specimen within the oil bath to regulate temperature from +65 °C to −20 °C. A thermocouple with an accuracy of 0.1 °C is mounted on the pedestal, which is linked to a chamber lid wrapped in thermal insulation. The sealed pressure vessel, rated to 32 MPa, sits in a load frame delivering 100 kN axial force via a hydraulic power pack; axial stress is captured by an internal load cell (0.1% FRO) that nullifies sidewall friction on the axial rod during triaxial shear.

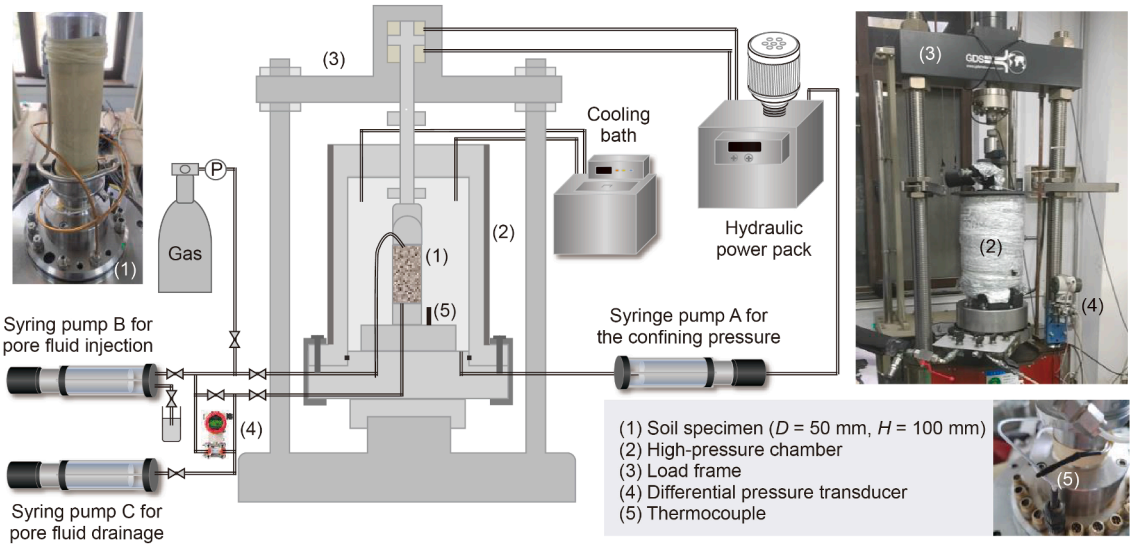

Fig. 1. A schematic of the experimental setup employed for hydrate-bearing sediments and physical appearances of the major components.

Axial displacement is tracked by a LVDT (Linear Variable Differential Transformer) with an accuracy of 0.1% FRO and a resolution of 0.2 μm. Specimen volume change under loading/unloading is resolved to 0.1 mm^3 by the confining pump, achieving volumetric accuracy better than 0.1%. Hydrate-forming gas is supplied from a high-pressure cylinder; water for flow tests is delivered by a syringe pump. A second syringe pump on the outlet maintains phase stability by precisely regulating pore pressure. Both pumps furnish up to 22.5 mL/min with ±0.5% accuracy. The differential pressure between inlet and outlet is monitored by an Asmik transducer (0–400 kPa, 0.075% FS). All parameters are logged automatically every 10 s through a data acquisition system.

As pore water reacting with clay minerals introduces extra variables into the hydraulic behavior of hydrate-free and hydrate-bearing sediments (Cao et al., 2024; Jang et al., 2018), standard quartz sands are employed as the host sediments in this study, and the grain-size distribution is displayed in Fig. 2. The median grain diameter d_{50} of the quartz sands is 170 μm, comparable to values reported by Suzuki et al. (2009) and marginally coarser than those supplied by Yoneda et al. (2015) for marine sediments hosting natural gas hydrates in the Nankai Trough. The minimum and maximum void ratios of the quartz sands, with a specific gravity of 2.65, are 0.533 and 0.935, respectively. In this study, distilled water and methane gas of 99.99% purity (Qingdao Dehaiweiye Technology Co., Ltd.) are utilized to synthesize methane hydrate within the host sediments.

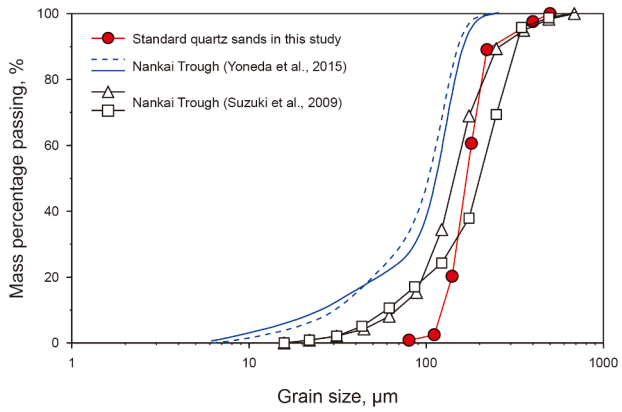

Fig. 2. Grain size distribution of the standard quartz sands employed in this study. The median grain diameter d_{50} is 170 μm. For marine sediments hosting natural gas hydrates in the Nankai Trough, d_{50} is tested to be 146 and 203 μm by Suzuki et al. (2009), and Yoneda et al. (2015) reported that d_{50} = 102 μm and d_{50} = 114 μm.

Air-dried quartz sands are blended with distill water at mass water contents of 1.8%, 2.2%, 5.3%, and 10.7%, and the moist sands are sealed in a plastic bag to cure for 8 h. Then, the mixture is evenly split into four portions by weight and carefully spooned into a sample mold one portion after another, followed by compaction on each portion to obtain a thickness of 25 mm. After the first three compaction steps, the entire top surface is thoroughly roughened to remove structural planes. The compacted moist sands together with the sample mold are placed into a freezer set at −5 °C for later use. The total mass of compacted moist sands is controlled to achieve a void ratio of 0.71, and the water content is predetermined according to the targeted hydrate saturation.

After several days of freezing, the frozen quartz sands are gently extruded from the sample mold by a custom hydraulic jack and cautiously positioned on the pedestal. Then, two rubber membranes separated by a tin-foil interlayer are fitted over the frozen sand sample, followed by placement of porous stones, filter papers, the top cap and flow-line connections. Thereafter, a confining pressure of 0.1 MPa is applied, and the ice is permitted to thaw at ambient temperature. Next, methane gas is steadily injected to elevate pore pressure at roughly 200 kPa/min, while confining pressure is concurrently increased to maintain a 200 kPa excess above pore pressure. Once pore pressure attains 7 MPa, methane injection is halted, and the temperature is reduced to 2 °C to initiate methane-hydrate formation in a sealed system. Throughout synthesis, pore pressure declines as methane is continuously consumed, and confining pressure is automatically lowered to keep the effective stress at an appropriate level. After pore pressure stabilized for over 12 h, hydrate formation is deemed complete, and the hydrate morphology is expected to be dominated by grain-coating (Zhang et al., 2023b). The residual gas is displaced by flushing precooled distilled water at 2 °C. During this displacement, a portion of the residual gas together with the incoming water converts into methane hydrate, and the remaining gas is considered fully expelled when no bubbles appear at the

outlet and the cumulative effluent water exceeds five times the initial pore volume. At this stage, fully saturated hydrate-bearing quartz-sand specimens are prepared; for hydrate-free specimens, the sole modification is the omission of methane-gas injection.

The saturated hydrate-bearing and hydrate-free specimens are isotropically loaded and unloaded under drained conditions with a maintained back-pressure. For each specimen, the effective stress (i.e., effective confining pressure) is increased from 0.2 to 20 MPa in nine steps (0.5, 1, 3, 5, 7, 10, 13, 15, and 18 MPa) and then decreased back to 0.2 MPa in seven steps (15, 10, 7, 5, 3, 1, and 0.5 MPa). At every effective-stress level, the specimen is allowed to consolidate until pore pressure equilibrates with the outlet pressure (set to 7 MPa in this study); consolidation is deemed complete once the volumetric change rate falls below 1 mm^3/min after each stress increment or decrement. Upon completion of consolidation, flow tests are conducted by flushing precooled distilled water at selected loading stages (1, 3, 5, 10, 15, and 20 MPa) and unloading stages (15, 10, 5, 3, and 1 MPa). During each test, the pressure difference between the inlet and outlet is held constant, with values ranging from 25 to 200 kPa depending on the condition; this range ensures a flushing rate that is both gentle enough to preserve specimen integrity and sufficiently high for reliable measurement (Xia et al., 2025). For each specific step and condition, the flushing procedure is repeated three to five times under slightly different pressure differences to verify repeatability. To focus on the mechanical and hydrodynamic controls, the temperature is held constant. After the isotropic loading-unloading cycle and all flow tests are completed, the methane hydrate is fully dissociated by heating; the entire volume of produced gas is collected and measured. It is noted that the maximum effective stress of 20 MPa adopted in this study corresponds to the modelled peak effective stress within the target reservoir in the Krishna-Godavari Basin (Myshakin et al., 2019) and also encompasses the actual peak effective stress experienced by the near-wellbore formation during the first field production trial in the Nankai Trough (Zhou et al., 2020b). Furthermore, the pressure difference for the flow tests is generated by lowering the outlet pressure rather than raising the inlet pressure, consistent with the depressurization method.

2.2. Calculation methods

The initial hydrate saturation S_{H0} prior to isotropic loading and unloading is calculated from the total volume V_{TM} of the produced gas, as follows:

$$S_{H0} = \frac{P_{atm} V_{TM}}{ZRT_r} \frac{M_H}{\rho_H V_s e_{0.2}} \tag{1}$$

where the symbol P_{atm} denotes the atmospheric pressure, R is the universal gas constant, T_r represents the thermodynamic temperature of the room (297.15 K), M_H denotes the molar mass of methane hydrate (124 g/mol), ρ_H is the density of methane hydrate (0.91 g/cm^3), V_s is the volume of sand particles (~114.8 cm^3), $e_{0.2}$ is the void ratio corresponding to an effective stress of 0.2 MPa, Z is the compressibility factor of methane gas, and $Z = 0.99823$ in this study according to the NIST (National Institute of Standards and Technology) database.

With respect to fluid flow in porous media, the effective void ratio e' is defined as the volume of pore space occupied by the fluid divided by the combined volume of the pore space occupied by solid hydrate and the soil particles. It is calculated as follows:

$$e' = \frac{(1 - S_H)e}{1 + S_H e} \tag{2}$$

where the symbol S_H stands for the hydrate saturation during isotropic loading and unloading, and e denotes the void ratio, defined as the volume ratio of the intrinsic pores over the soil particles.

The effective absolute permeability K of hydrate-bearing quartz sands is determined based on Darcy's law, with the calculation equation as follows:

$$K = \frac{\mu_w Q H}{A(P_{in} - P_{out})} \tag{3}$$

where the symbol μ_w stands for the dynamic viscosity of water at 2 °C (1.6728×10^{-3} Pa·s), and Q denotes the water-flushing rate. P_{in} and P_{out} represent the inlet and outlet pressures, respectively. The cross-sectional area A and height H of the specimen vary with changes in effective stress and are determined from the specimen volume and vertical deformation (Zhang et al., 2022).

The permeability-stress-sensitivity coefficient η is defined as

$$\eta = -\frac{1}{K}\frac{\partial K}{\partial p'} \tag{4}$$

where the symbol p' represents the mean effective stress and, in this study, equals the effective confining pressure σ'. In practice, a discrete form of Eq. (4) is employed:

$$\eta(p'_{i+1}) = \eta(p'_i \rightarrow p'_{i+1}) = -\frac{1}{K(p'_i)} \frac{K(p'_{i+1}) - K(p'_i)}{p'_{i+1} - p'_i} \tag{5}$$

where the subscription "i" refers to the current mean effective stress, and "i+1" to the subsequent value during isotropic loading; the symbol $K(p'_i)$ is the effective absolute permeability at the current stress level.

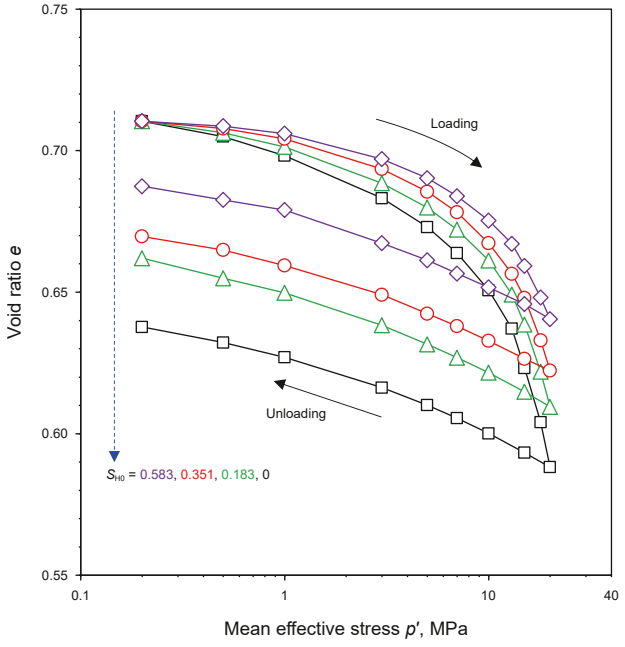

Fig. 3. Changes in the void ratio of hydrate-bearing and hydrate-free quartz sands under isotropic loading and unloading. The symbol S_{H0} represents the initial hydrate saturation which is calculated from Eq. (1).

3. Results

3.1. Void ratio and the effective void ratio

Fig. 3 presents the void-ratio evolution of hydrate-free and hydrate-bearing quartz sands under isotropic loading and unloading; every value is recorded after full consolidation at each load step. For hydrate-free sands, the void ratio falls from 0.710 to 0.588 (i.e., a 17.2% compression) as the mean effective stress rises from 0.2 to 20 MPa, and rebounds to 0.638 (i.e., a 10.1% net compression) once the stress is unloaded back to 0.2 MPa. For hydrate-bearing sands, the initial void ratio is likewise 0.710, yet at every load stage the void ratio remains higher than that of the hydrate-free counterpart, unequivocally indicating the stiffening action of pore-occupied methane hydrate. While the mean effective stress climbs from 0.2 to 20 MPa, the void ratio drops to 0.610 at S_{H0} = 0.183, to 0.622 at S_{H0} = 0.351, and to 0.641 at S_{H0} = 0.583, equivalent to compressions of 14.1%, 12.4%, and 9.7%, respectively. Upon unloading to 0.2 MPa, the void ratio recovers to 0.662 at S_{H0} = 0.183, to 0.670 at S_{H0} = 0.351, and to 0.687 at S_{H0} = 0.583, corresponding to residual compressions of 6.8%, 5.6%, and 3.2%, respectively. These trends plainly illustrate that skeleton compressibility attenuates with growing methane hydrate saturation, and that post-cycle residual deformation diminishes as initial hydrate saturation increases, corroborating the pore-scale stiffening role of methane hydrate.

Owing to void-ratio evolution during isotropic loading and unloading, hydrate saturation shifts with the mean effective stress, as depicted in Fig. 4(a). When the mean effective stress rises from 0.2 to 20 MPa, hydrate saturation climbs to 0.213 for the initial hydrate saturation S_{H0} = 0.183, to 0.401 for S_{H0} = 0.351, and to 0.647 for S_{H0} = 0.583, representing increases of 16.4%, 14.2%, and 11.0%, respectively. After unloading back to 0.2 MPa, hydrate saturation falls yet remains above the initial hydrate saturation, corresponding to residual increases of 7.1%, 6.0%, and 3.4%, respectively. It is evident that the extent of hydrate-saturation increases induced by mean-effective-stress changes diminish at higher initial hydrate saturations. Integrating the concurrent variations in void ratio and hydrate saturation during isotropic loading and unloading, the evolution of the effective void ratio with the mean effective stress is presented in Fig. 4(b). For both hydrate-free and hydrate-bearing quartz sands, as the mean effective stress increases from 0.2 to 20 MPa, the effective void ratio decreases from 0.710 to 0.588 for S_{H0} = 0, from 0.514 to 0.424 for S_{H0} = 0.183, from 0.369 to 0.299 for S_{H0} = 0.351, and from 0.210 to 0.160 for S_{H0} = 0.583, corresponding to compressions of 17.2%, 17.5%, 19.0%, and 23.8%, respectively. Upon unloading to 0.2 MPa, the effective void ratio rebounds to 0.638 for S_{H0} = 0, to 0.471 for S_{H0} = 0.183, to 0.337 for S_{H0} = 0.351, and to 0.193 for S_{H0} = 0.583, corresponding to residual compressions of 10.1%, 8.4%, 8.7%, and 8.1%, respectively. It is clear that the compression magnitude of the effective void ratio after virgin loading grows with rising initial hydrate saturation; by contrast, the compression magnitude based on the void ratio diminishes with rising initial hydrate saturation. After a complete loading-unloading cycle, both the compression magnitude of the effective void ratio and that of the void ratio declines as the pore content of methane hydrate increases.

3.2. Effective absolute permeability and coefficient of the permeability stress sensitivity

Fig. 5(a) illustrates the evolution of effective absolute permeability with the mean effective stress during isotropic loading and unloading. For hydrate-free quartz sands, the effective absolute permeability declines from 234.0 to 40.2 mD as the mean effective stress rises from 1 to 20 MPa, and upon unloading back to 1 MPa, it marginally recovers to 53.5 mD, yielding a cyclic permeability damage ratio of 77.1%. For hydrate-bearing quartz sands, as the mean effective stress increases from 1 to 20 MPa and then unloads to 1 MPa, the effective absolute permeability falls from 40.5 to 5.6 mD and rebounds to 13.4 mD for S_{H0} = 0.183, from 18.1 to 0.75 mD and rebounds to 5.8 mD for S_{H0} = 0.351, from 7.4 to 0.26 mD and rebounds to 3.6 mD for S_{H0} = 0.583, corresponding to permeability damage ratios of 66.9%, 68.0%, and 51.4%, respectively. Overall, the

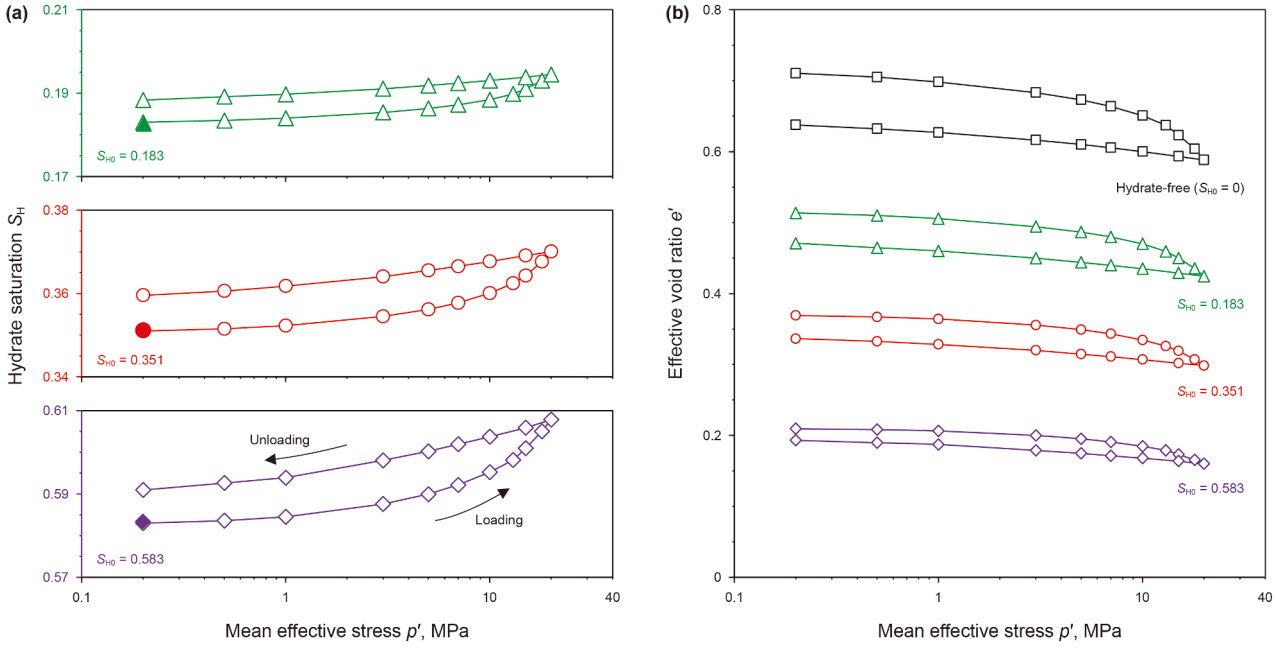

Fig. 4. Changes in hydrate saturation of hydrate-bearing quartz sands (**a**) and the effective void ratio of hydrate-bearing as well as hydrate-free quartz sands (**b**) under isotropic loading and unloading. The symbol S_{H0} represents the initial hydrate saturation, and the effective void ratio is calculated from Eq. (2). The initial effective void ratio is 0.710, 0.514, 0.369, and 0.210 for S_{H0} = 0, 0.183, 0.351, and 0.583, respectively.

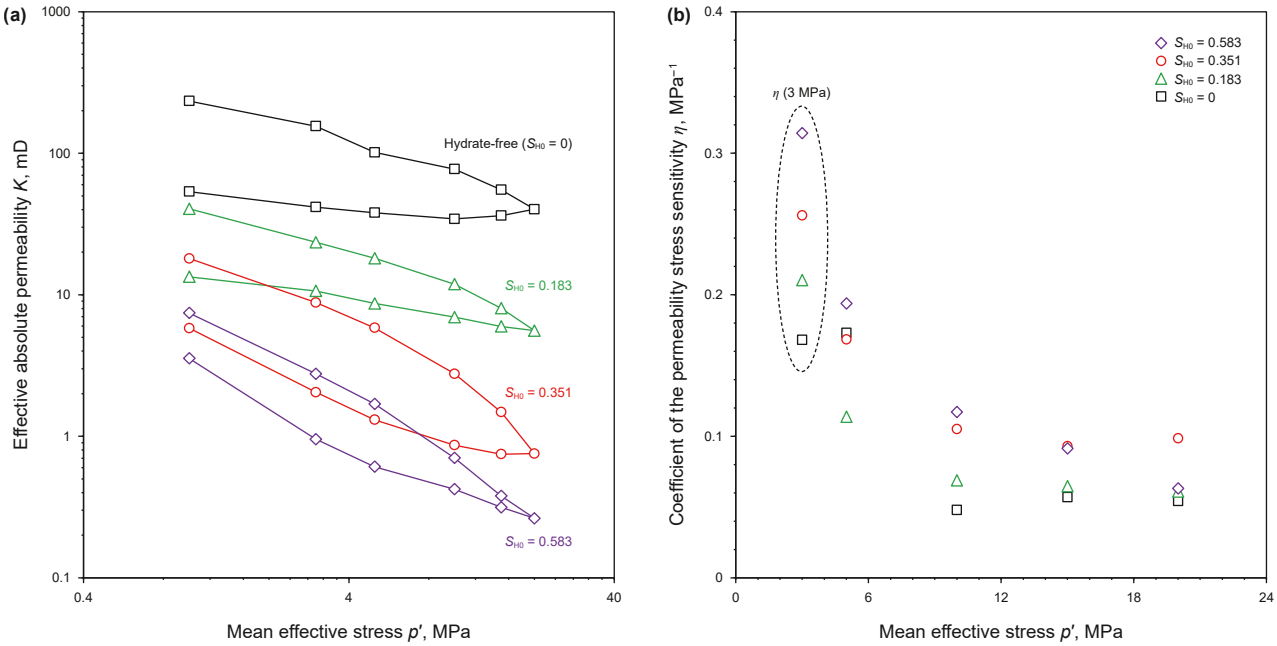

Fig. 5. Changes in the effective absolute permeability (**a**) and the permeability stress sensitivity coefficient (**b**) of hydrate-bearing and hydrate-free quartz sands. The symbol S_{H0} is the initial hydrate saturation, and coefficient of the permeability stress sensitivity is calculated from Eq. (5). The effective absolute permeability at a mean effective stress of 1 MPa is 234.0, 40.5, 18.1, and 7.4 mD for $S_{H0} = 0$, 0.183, 0.351, and 0.583, respectively.

permeability damage ratio induced by isotropic loading and unloading diminishes with rising initial hydrate saturation. The coefficient of permeability stress sensitivity during isotropic loading is depicted in Fig. 5(b). It reveals that the coefficient for both hydrate-free and hydrate-bearing quartz sands across all initial hydrate saturations generally decreases with increasing mean effective stress, implying that higher stresses attenuate permeability sensitivity. This trend is further highlighted in Fig. 6(a), which presents the permeability stress sensitivity coefficient normalized by the value enclosed in the dotted ellipse in Fig. 5(b); the overall pattern is well captured by the following equation:

$$H_S = \frac{\eta}{\eta(3\ \mathrm{MPa})} = \left(1 + \ln\left(\frac{\sigma'}{3\ \mathrm{MPa}}\right)\right)^a \tag{6}$$

where the symbol a is an empirical index which quantitatively dictates both the direction and the magnitude of how the

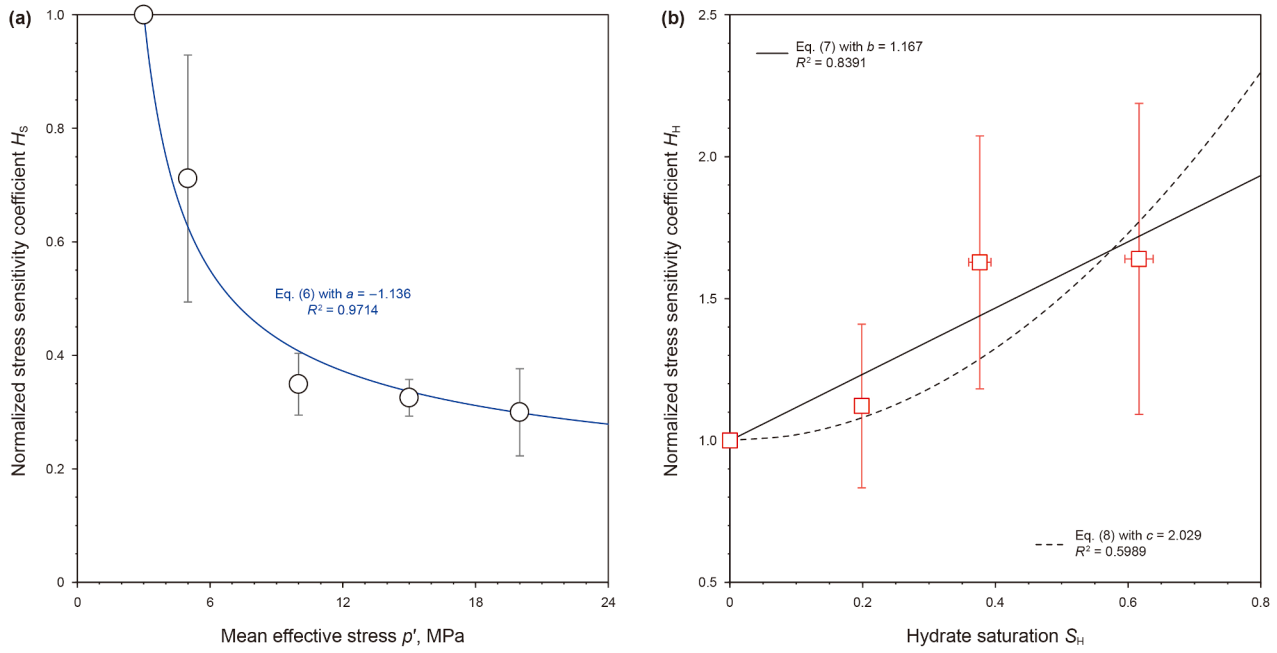

Fig. 6. Normalized coefficients H_S (**a**) and H_H (**b**) of the permeability stress sensitivity. Open black circles and red squares stand for experimental data in this study. The blue solid curve is plotted according to Eq. (6), and the black solid line is drawn based on Eq. (7). The black dashed curve is plotted according to Eq. (8).

permeability stress sensitivity evolves with changing mean effective stress, and its value is fitted as −1.136 in this study. Fig. 6(b) displays the permeability stress sensitivity coefficient normalized by that of hydrate-free quartz sands, and the overall trend with hydrate saturation is captured by the following equation:

$$H_{\mathrm{H}} = \frac{\eta(S_{\mathrm{H}})}{\eta(S_{\mathrm{H}}=0)} = 1 + b \cdot S_{\mathrm{H}} \tag{7}$$

where the symbol b is an empirical parameter, and its value is fitted as 1.167 in this study. For the normalized permeability stress sensitivity evolving with hydrate saturation, Zhang et al. (2022) propose an empirical equation of the following form:

$$H_{\mathrm{H}} = 1 + c \cdot (S_{\mathrm{H}})^2 \tag{8}$$

where the symbol c is an empirical parameter, and its value is fitted as 2.039 in this study. However, the coefficient of determination for Eq. (8) is markedly lower than that for Eq. (7). It is evident that empirical parameters b and c quantify the direction and strength with which hydrate saturation modifies the permeability stress sensitivity in hydrate-bearing sediments.

4. Analyses and discussion

4.1. A model of the void ratio in hydrate-bearing sands during isotropic loading and unloading

It has been demonstrated that the pore-hosted methane hydrate modifies the void-ratio evolution of hydrate-bearing sands under isotropic loading and unloading. Quantifying this hydrate influence begins with one of the simplest formulations that capture the stress dependence of the void ratio for unsaturated soils devoid of gas hydrates, expressed as follows:

$$e = e_0 - \alpha_{\mathrm{p}} \ln\left(1 + \frac{p'}{P_{\mathrm{r}}}\right) - \alpha_{\mathrm{s}} \ln\left(1 + \frac{s}{P_{\mathrm{atm}}}\right) \tag{9}$$

where the symbol p' denotes mean effective stress, s denotes matrix suction, e_0 denotes the initial void ratio prior to changes in mean effective stress and matrix suction, P_{r} denotes a reference pressure, α_{p} denotes soil compressibility with respect to mean effective stress, and α_{s} denotes soil compressibility with respect to matrix suction. Eq. (9) is widely incorporated in constitutive models for unsaturated soils—for example, Alonso et al. (1990)—and has also been employed in the development of water-retention models (Chang and Zhou, 2025; Cheng et al., 2019; Cui et al., 2025; Zhou and Ng, 2014). In this study, the specimens are water saturated with water, so Eq. (9) is simplified as follows:

$$e = e_0 - \alpha_{\mathrm{p}} \ln\left(1 + \frac{p'}{P_{\mathrm{r}}}\right) \tag{10}$$

where the parameter α_{p} equals the compression index λ under isotropic loading and the swelling index κ under isotropic unloading. Because theoretical analyses (Uchida et al., 2012) and experimental data (Hyodo et al., 2013; Yan et al., 2023; Zhou et al., 2021) indicate that λ and κ are essentially independent on hydrate saturation, these two indices for hydrate-bearing sands are taken identical to those for hydrate-free sands in this study, while the reference pressure P_{r} is treated as a hydrate-saturation-dependent parameter.

Fig. 7(a) presents the fitting outcome obtained with Eq. (10) for hydrate-free quartz sands under isotropic loading. The reference pressure P_{r} is 55.73 MPa, and the compression index λ is 0.3685. With λ fixed at 0.3685, the fitting results for hydrate-bearing quartz sands at initial hydrate saturations of 0.183 and 0.351 are displayed in Fig. 7(b) and (c), respectively. The reference pressure P_{r} is 66.48 MPa for $S_{\mathrm{H0}} = 0.183$ and 77.39 MPa for $S_{\mathrm{H0}} = 0.351$. It is evident that the reference pressure P_{r} rises with the growing presence of methane hydrate in pores, and this trend is accurately captured by the following linear equation:

$$\frac{P_{\mathrm{r}}(S_{\mathrm{H0}})}{P_{\mathrm{r}}(S_{\mathrm{H0}}=0)} = 1 + d \cdot S_{\mathrm{H0}} \tag{11}$$

where the fitting parameter d quantifies how strongly hydrate saturation alters the reference pressure (and hence the mechanical stiffness) of hydrate-bearing sediments, with its magnitude tied directly to the dominant hydrate morphology, and its value is 1.264 in this study (Fig. 7(d)).

For hydrate-free quartz sands subjected to unloading, Eq. (10) remains applicable, and the fitting outcome is displayed in Fig. 8(a) with $e_0 = 0.638$. The reference pressure P_{r} is 1.349 MPa, and the swelling index is 0.0178, which is likewise fixed for hydrate-bearing sands (Fig. 8(b) and (c)). The parameter e_0 equals 0.662 for $S_{\mathrm{H0}} = 0.183$ and 0.670 for $S_{\mathrm{H0}} = 0.351$. Correspondingly, the reference pressure P_{r} is 1.122 MPa for $S_{\mathrm{H0}} = 0.183$ and 1.439 MPa for $S_{\mathrm{H0}} = 0.351$. As illustrated in Fig. 8(d), the reference pressure P_{r} for unloading fluctuates with increasing initial hydrate saturation, averaging 1.303 MPa, which yields a zero fitting parameter in Eq. (11).

For the initial hydrate saturation of 0.583, the reference pressure P_{r} under isotropic loading is calculated from Eq. (11) as 96.80 MPa, and this value is then applied to predict the void ratio via Eq. (10). The predicted void ratio plotted in Fig. 9(a) aligns closely with the measured values, with deviations confined within ±1%. Likewise, the reference pressure P_{r} during unloading is 1.303 MPa, and the corresponding predictions in Fig. 9(b) ($e_0 = 0.687$) also match the measured void ratio, again with errors held within ±1%.

4.2. Positive and negative effects of methane hydrate with respect to the effective pore volume

Fig. 3 demonstrates that, under an identical mean effective stress, the void ratio in both hydrate-free and hydrate-bearing quartz sands rises with increasing initial hydrate saturation. Conversely, Fig. 4(b) reveals that the effective void ratio declines as the initial hydrate saturation increases. This contrast confirms that pore-occupied methane hydrate concurrently exerts positive and negative influences on the effective pore volume evolution with the mean effective stress.

During isotropic loading, the void ratio of hydrate-bearing quartz sands at an initial hydrate saturation of 0.183 is replotted in Fig. 10(a) as open blue triangles. In the absence of methane hydrate in pores, the void ratio would coincide with that of hydrate-free quartz sands, shown in Fig. 10(a) as open black squares. The yellow delta-shaped region denotes the positive strengthening effect of methane hydrate on effective pore volume change. The effective void ratio of hydrate-bearing quartz sands with an initial hydrate saturation of 0.183 is plotted as solid blue triangles in Fig. 10(b). Ignoring the hydrate-saturation shift caused by isotropic loading (Fig. 4(a)), the effective void ratio would follow the dashed blue curve in Fig. 10(b). The gray delta-shaped region signifies the enhanced filling effect of methane hydrate arising from compression. The gap between the open blue triangles in Fig. 10(a) and the solid blue triangles in Fig. 10(b) quantifies the negative effect of methane hydrate on effective pore volume change, encompassing both the normal and the enhanced

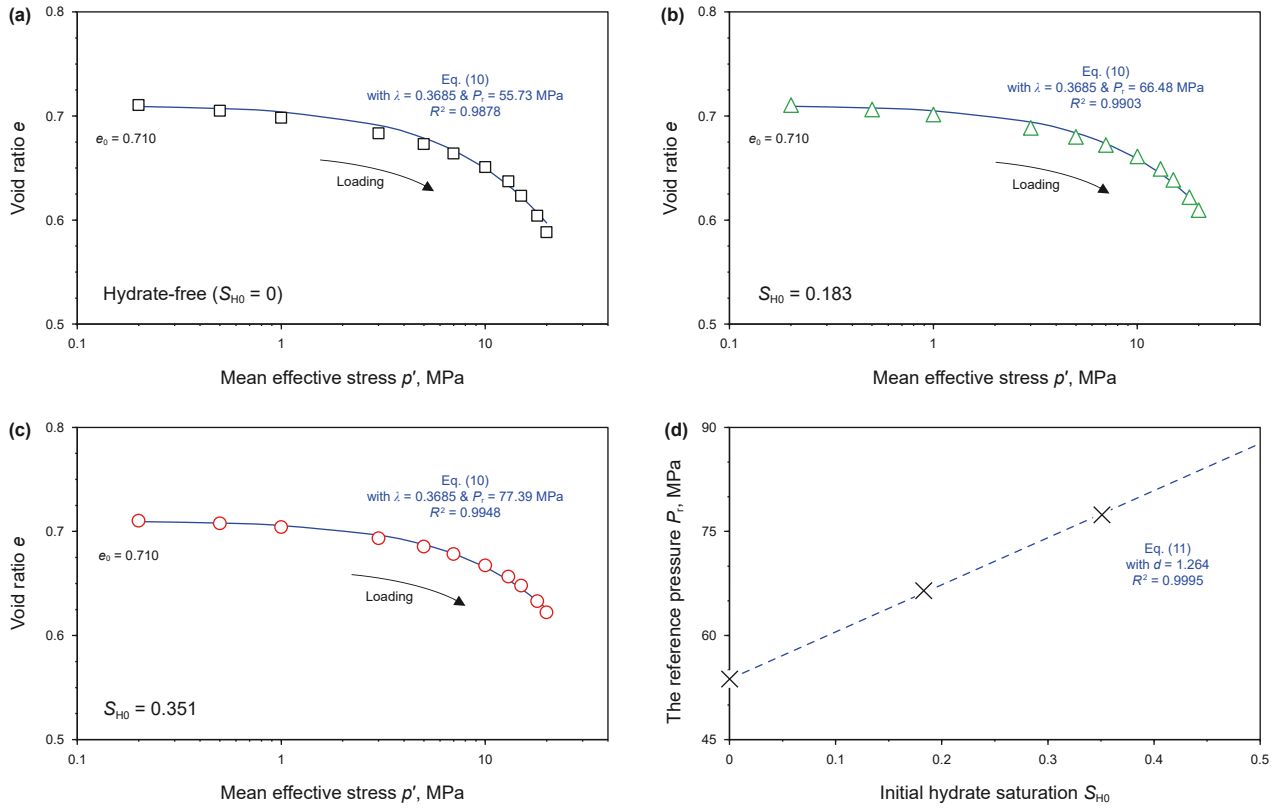

Fig. 7. Changes in the void ratio of hydrate-free (**a**) and hydrate-bearing (**b**, **c**) quartz sands under isotropic loading and the reference pressure (**d**) changing with the initial hydrate saturation. Open dots with different colors represent the experimental data, and the solid curve with blue color is drawn from Eq. (10) with different values of the reference pressure. The compression index $\lambda = 0.3658$ in this study. The dashed blue line is drawn from Eq. (11) with a fitting parameter $d = 1.264$.

filling contributions. Analogous curves for hydrate-bearing quartz sands at higher initial hydrate saturations (i.e., 0.351 and 0.583) are displayed in Fig. 10(c)–(f). It is evident that both the strengthening (i.e., yellow region) and the enhanced filling (i.e., gray region) effects of methane hydrate intensify as the pore content of methane hydrate increases.

To quantify the positive and negative impacts of methane hydrate, three coefficients are introduced. The first, termed the strengthening effect coefficient R_s, captures the positive contribution and is defined as follows:

$$R_s = \frac{\int_{p_0'}^{p'} (e(S_{H0}) - e(S_{H0}=0))\mathrm{d}p'}{p'} \tag{12}$$

where the symbol p_0' denotes the initial mean effective stress (set at 0.2 MPa in this study), $e(S_{H0})$ is the void ratio of hydrate-bearing quartz sands (i.e., the blue triangles in Fig. 10(a), the red circles in Fig. 10(c), and the purple diamonds in Fig. 10(e), and $e(S_{H0}=0)$ is the void ratio of hydrate-free quartz sands (i.e., the black squares in Fig. 10(a)–(c), and (e)). The second coefficient, the normal filling effect coefficient R_n, quantifies part of the negative effect and is expressed as follows:

$$R_n = \frac{\int_{p_0'}^{p'} (e'(S_{H0}) - e(S_{H0}))\mathrm{d}p'}{p'} \tag{13}$$

where the symbol $e'(S_{H0})$ denotes the effective void ratio of hydrate-bearing quartz sands, calculated without accounting for the change in hydrate saturation caused by compression (i.e., the dashed curves in Fig. 10(b), (d), and 10(f)). The third coefficient, the enhanced filling effect coefficient R_e, captures the remaining negative influence and is defined as follows:

$$R_e = \frac{\int_{p_0'}^{p'} (e'(S_H) - e'(S_{H0}))\mathrm{d}p'}{p'} \tag{14}$$

where the symbol $e'(S_H)$ denotes the effective void ratio of hydrate-bearing quartz sands accounting for hydrate-saturation change caused by compression (i.e., the blue triangles in Fig. 10(b), the red circles in Fig. 10(d), and the purple diamonds in Fig. 10(f)). By definition, these three coefficients in Eqs. (12)–(14) are dimensionless, and their sum is defined as the total effect coefficient $R_t = R_s + R_n + R_e$ governing the effective pore volume.

Fig. 11(a) illustrates the strengthening effect coefficient R_s of hydrate-bearing quartz sands versus the mean effective stress. The coefficient R_s rises with increasing mean effective stress, and, at any given stress, it also rises with increasing initial hydrate saturation. Fig. 11(b) presents the normal filling effect coefficient R_n under various mean effective stresses; the negative sign denotes an adverse influence. The coefficient R_n is essentially independent of the mean effective stress, yet its absolute magnitude grows with increasing initial hydrate saturation, reflecting a stronger effect as methane hydrate content increases. Fig. 11(c) depicts the enhanced filling effect coefficient R_e; its absolute value escalates with both the mean effective stress and the initial hydrate saturation. Notably, the absolute value of R_n is one order of magnitude larger than both the absolute values of R_s and R_e, highlighting the dominance of the normal filling effect. This conclusion is reinforced in Fig. 11(d), where the total effect coefficient R_t is displayed.

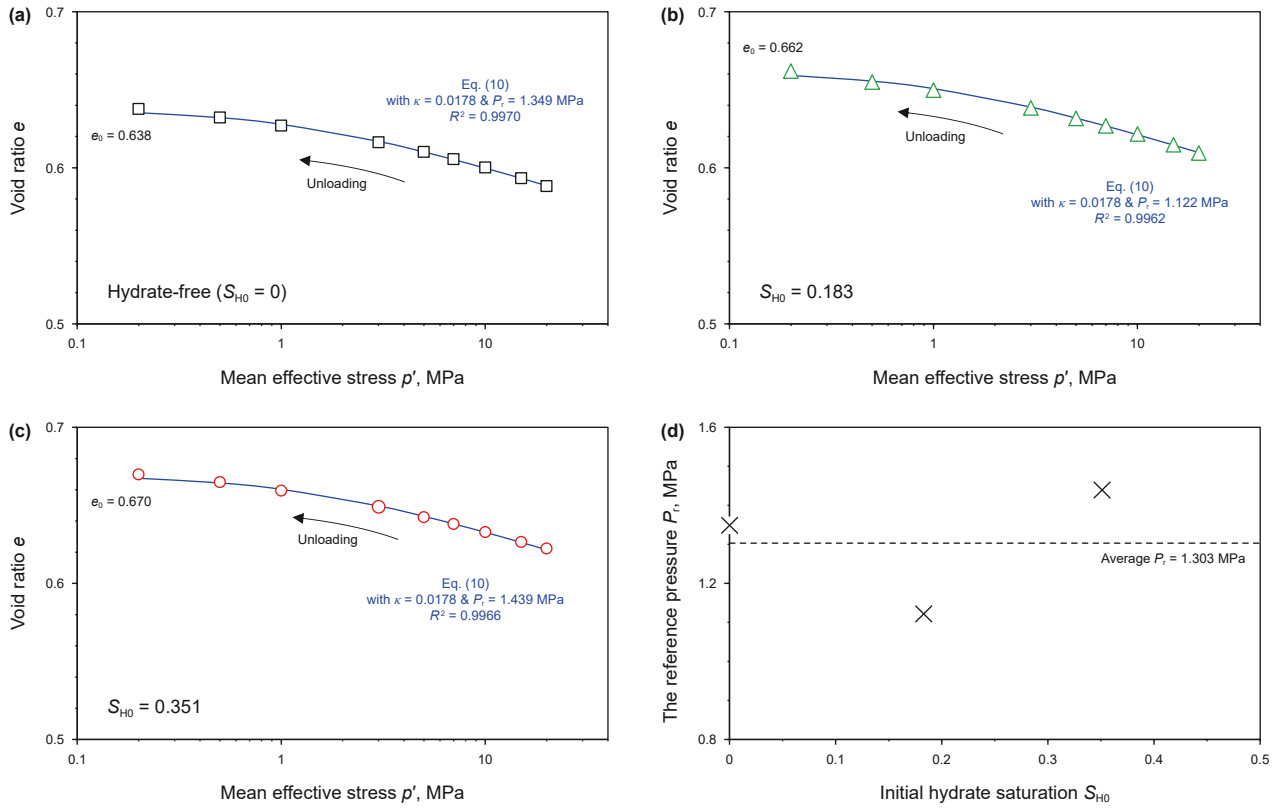

Fig. 8. Changes in the void ratio of hydrate-free (**a**) and hydrate-bearing (**b**, **c**) quartz sands under isotropic unloading and the reference pressure (**d**) changing with the initial hydrate saturation. Open dots with different colors represent the experimental data, and the solid curve with blue color is drawn from Eq. (10) with different values of the initial void ratio and the reference pressure. The swelling index $\kappa = 0.0178$ in this study. The dashed black line stands for the average value of the reference pressure.

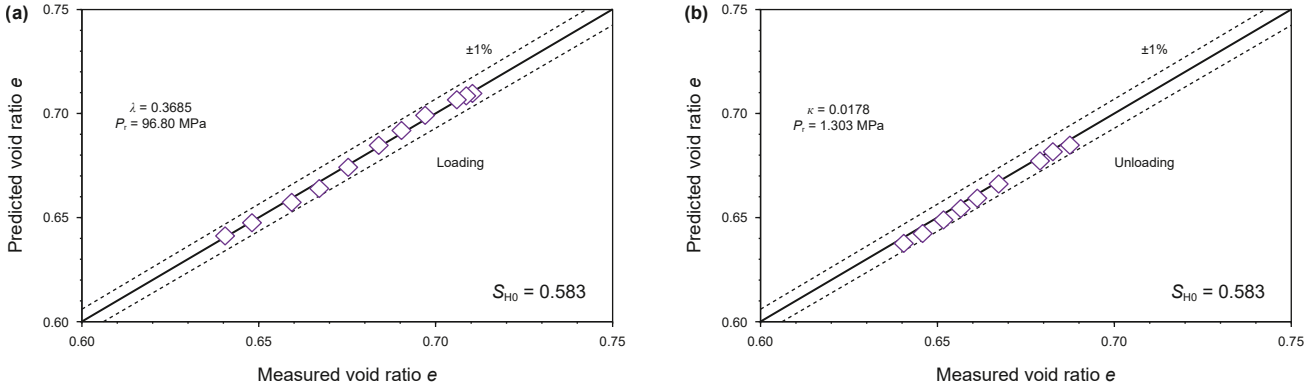

Fig. 9. Comparisons between the predicted and measured void ratio of hydrate-bearing quartz sands under isotropic loading (**a**) and unloading (**b**). The initial hydrate saturation is 0.583. Value of the reference pressure with respect to isotropic loading $P_r = 96.80$ MPa is calculated from Eq. (11), and value of the reference pressure with respect to isotropic unloading $P_r = 1.303$ MPa is consistent with the average value shown in Fig. 8(d).

As Fig. 12 illustrates, magnitudes of those three coefficients scale with initial hydrate saturation; their physical underpinning is captured by the simple relation:

$$R_s, R_n, R_e = m_1 \sqrt{S_{H0}} \tag{15}$$

where m_1 is a fitting parameter. Values of m obtained are 0.01787 for the strengthening effect coefficient R_s (Fig. 12(a)), −0.5613 for the normal filling effect coefficient R_n (Fig. 12(b)), and −0.01274 for the enhanced filling effect coefficient R_e (Fig. 12(c)). For the total effect coefficient R_t, m_1 equals −0.5562 (Fig. 12(d)), nearly identical to that for R_n, confirming that the dominant influence on effective pore volume is the normal filling effect of methane hydrate.

4.3. Positive and negative effects of methane hydrate with respect to the effective absolute permeability

The effective absolute permeability of both hydrate-free and hydrate-bearing quartz sands in this study is correlated with the effective void ratio through:

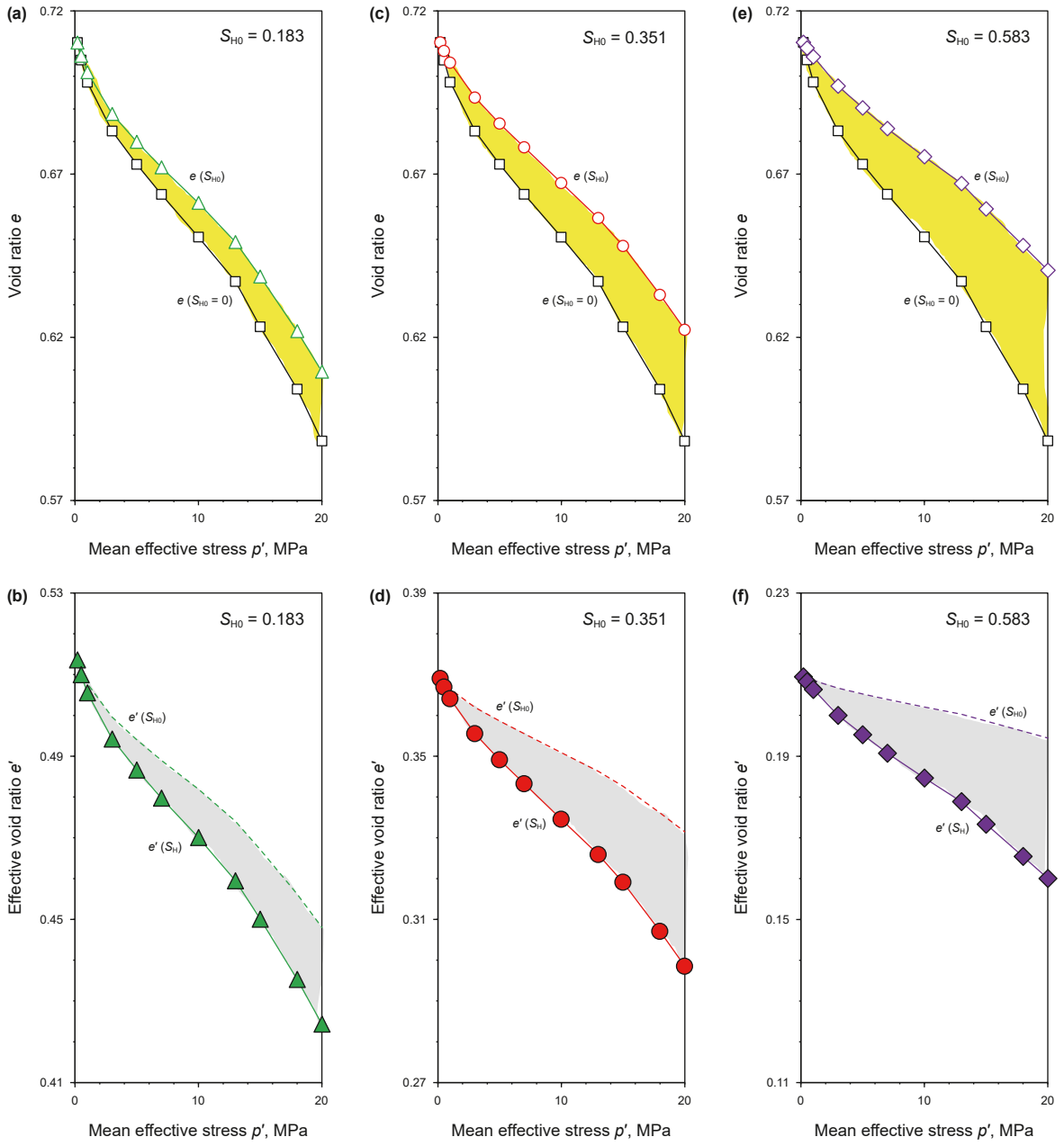

Fig. 10. Changes in the void ratio and the effective void ratio of hydrate-bearing quartz sands under isotropic loading. The initial hydrate saturation is 0.183 (**a**, **b**), 0.351 (**c**, **d**), and 0.583 (**e**, **f**). The open black squares in (a), (c), (e) represent the void ratio of hydrate-free sands. The open blue triangles in (a), red circles in (c), and purple diamonds in (e) stand for the void ratio of hydrate-bearing sands. The dashed curves with blue in (b), red in (d), and purple in (f) colors stand for the effective void ratio of hydrate-bearing sands calculated without considering the variation of hydrate saturation. The solid blue triangles in (b), red circles in (d), and purple diamonds in (f) represent the effective void ratio of hydrate-bearing sands calculated with the variation of hydrate saturation being included.

$$\log\left(\frac{K}{1\ \mathrm{mD}}\right) = n_1(e')^2 + n_2(e') + n_3 \tag{16}$$

where n_1, n_2, and n_3 are empirical parameters whose values—together with the corresponding coefficients of determination—are listed in Table 1. Because the void-ratio range of hydrate-bearing quartz sands under isotropic loading (Fig. 3) falls well within the calibration range of Eq. (16) for hydrate-free sands (Table 1), the host-sediment effective absolute permeability is assumed to follow Eq. (16) with $n_1 = 66.7$, $n_2 = -79.2$, and $n_3 = 25.1$. Likewise, the effective void ratios calculated for hydrate-bearing sands while ignoring hydrate-saturation change also lie within the applicable ranges of Eq. (16) for hydrate-bearing cases (Table 1); hence, the effective absolute permeability of hydrate-bearing quartz sands—evaluated with an effective void ratio that neglects hydrate-saturation change—is likewise assumed to obey Eq. (16) using the corresponding parameter set.

Fig. 13(a)–(c) present the evolution of the effective absolute permeability K_{hs} of the host sediments as open blue triangles ($S_{H0} = 0.183$), red circles ($S_{H0} = 0.351$), and purple diamonds ($S_{H0} = 0.583$), respectively. Open black squares denote the effective absolute permeability K_{hf} of hydrate-free quartz sands. It is evident that K_{hs} for hydrate-bearing quartz sands exceeds K_{hf}, and the yellow delta-shaped region quantifies the positive influence of

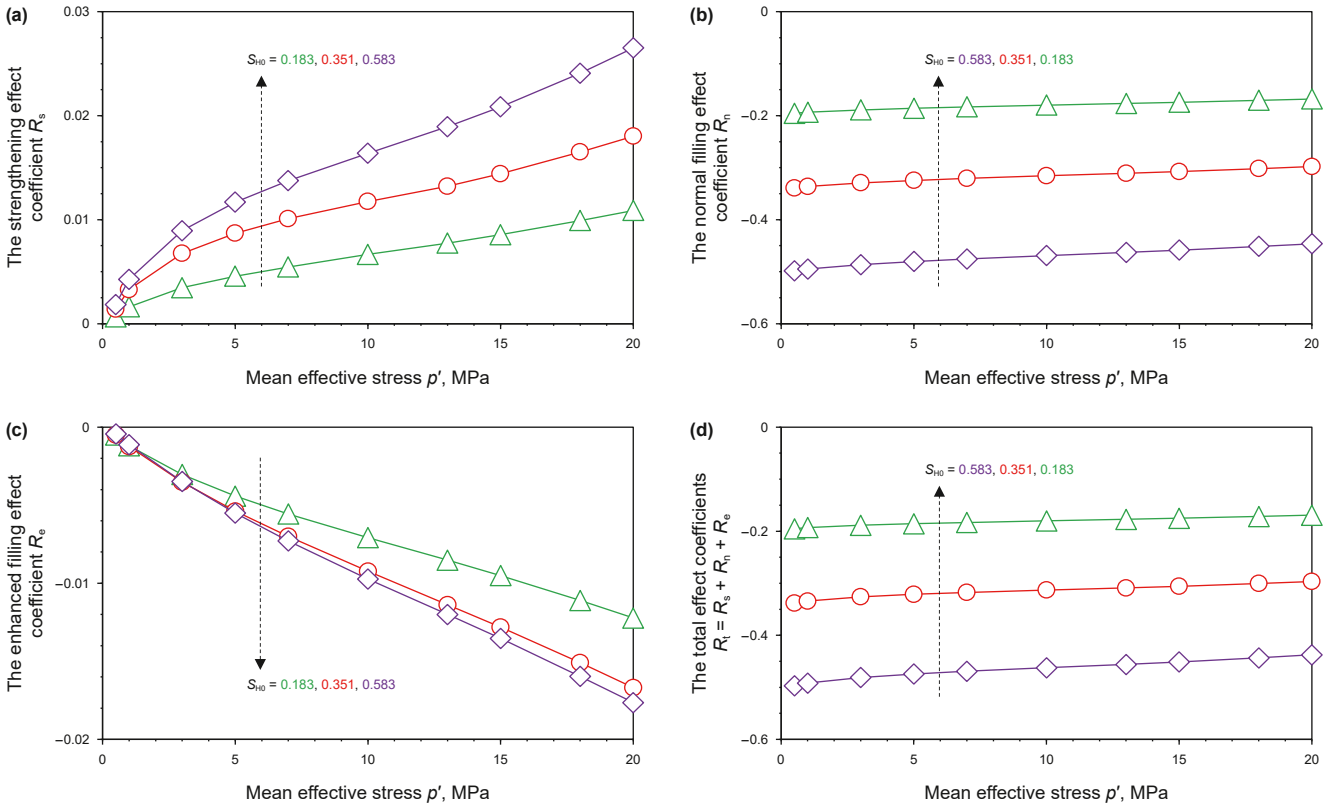

Fig. 11. Changes in the strengthening effect coefficient (**a**), the normal filling effect coefficient (**b**), the enhanced filling effect coefficient (**c**), and the total effect coefficient (**d**) of hydrate-bearing quartz sands under isotropic loading. The initial hydrate saturation is 0.183, 0.351, and 0.583 in this study.

methane hydrate on effective absolute permeability. Fig. 13(b), (d), and 13(f) illustrate the effective absolute permeability K_{uh} of hydrate-bearing quartz sands when hydrate-saturation changes caused by compression are ignored, shown as dashed blue ($S_{H0} = 0.183$), red ($S_{H0} = 0.351$), and purple ($S_{H0} = 0.583$) curves. In these panels, the effective absolute permeability K_{hb} of hydrate-bearing quartz sands that accounts for compression-induced hydrate-saturation changes is plotted as solid blue triangles ($S_{H0} = 0.183$), red circles ($S_{H0} = 0.351$), and purple diamonds ($S_{H0} = 0.583$). The gray delta-shaped region represents the compression-enhanced filling effect of methane hydrate, which is detrimental to effective absolute permeability. The effective absolute permeability K_{hf} and K_{hb} is directly measured, whereas K_{hs} and K_{uh} cannot be measured and are instead computed from Eq. (16) using the corresponding fitting parameters listed in Table 1.

To quantify the positive and negative influences of methane hydrate on effective absolute permeability, three coefficients—analogous to those for the effective void ratio—are defined as:

$$Y_s = \frac{\int_{p'_0}^{p'} \left(K_{hs} - K_{hf}\right) dp'}{p'} \tag{17}$$

$$Y_n = \frac{\int_{p'_0}^{p'} \left(K_{uh} - K_{hs}\right) dp'}{p'} \tag{18}$$

$$Y_e = \frac{\int_{p'_0}^{p'} \left(K_{hb} - K_{uh}\right) dp'}{p'} \tag{19}$$

where Y_s, Y_n, and Y_e denote the strengthening, the normal filling, and the enhanced filling effect coefficients governing effective absolute permeability, respectively. The sum of these three coefficients defines the total effect coefficient Y_t with respect to the effective absolute permeability.

Fig. 14(a)–(c) illustrate the evolution of the strengthening effect Y_s, the normal filling effect Y_n, and the enhanced filling effect Y_e coefficients governing effective absolute permeability; the negative sign denotes a positive contribution. All three effects intensify as the initial hydrate saturation rises, and their physical dependence is captured by:

$$\left(\frac{Y_s}{1\ \text{mD}}\right), \left(\frac{Y_n}{1\ \text{mD}}\right), \left(\frac{Y_e}{1\ \text{mD}}\right) = m_2 \sqrt{S_{H0}} \tag{20}$$

where fitting parameters $m_2 = 63.01$ for Y_s, $m_2 = -314.3$ for Y_n, and $m_2 = -5.898$ for Y_e. Eq. (20) also applies to the total effect coefficient Y_t, whose fit is displayed in Fig. 14(d); the overall trend of Y_t closely mirrors that of Y_n (Fig. 14(b)), confirming that the normal filling effect of methane hydrate dominates the effective-absolute-permeability response to isotropic loading.

To compare the positive and negative influences of methane hydrate on both the effective void ratio and the effective absolute permeability, two dimensionless coefficients are introduced:

$$N_E = \frac{R_s}{\text{abs}(R_n + R_e)} \tag{21}$$

$$N_K = \frac{Y_s}{\text{abs}(Y_n + Y_e)} \tag{22}$$

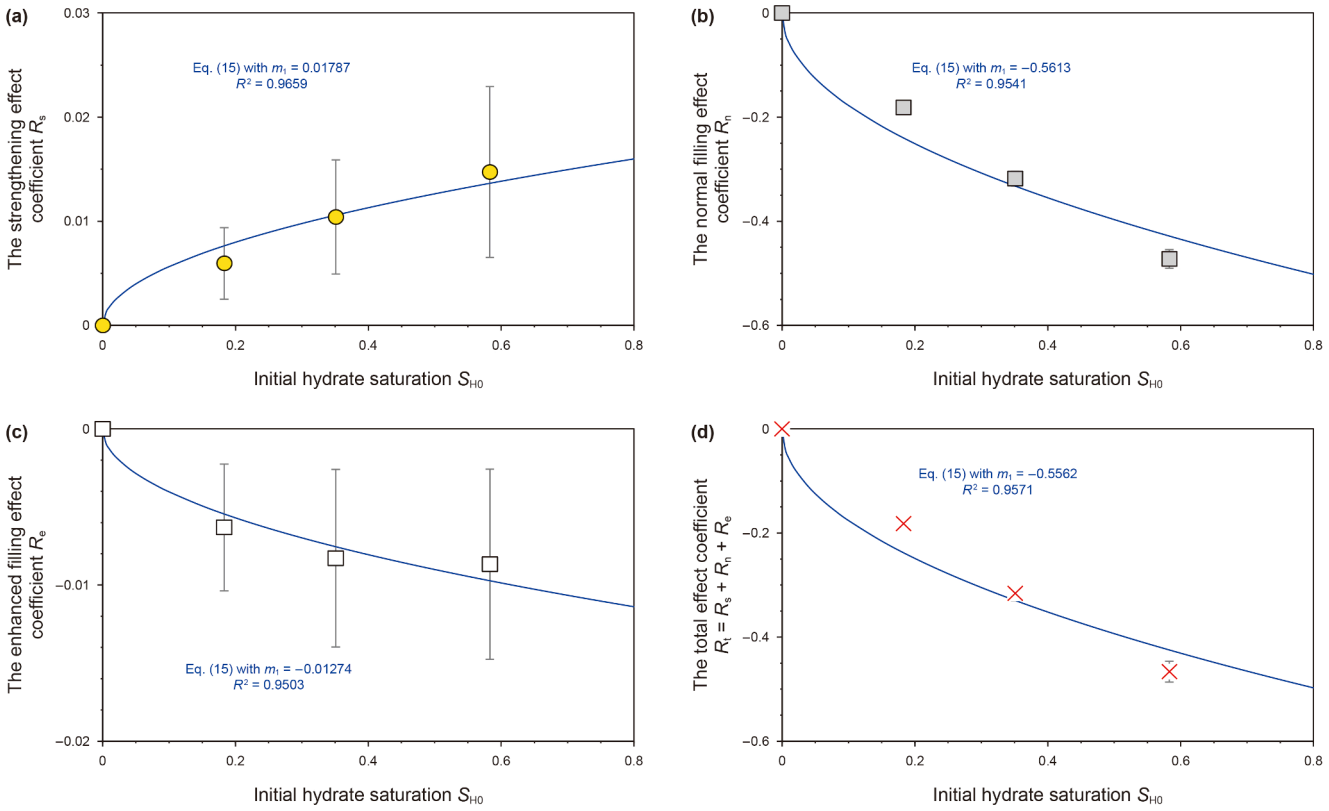

Fig. 12. With respect to the effective void ratio, changes in the strengthening effect coefficient (**a**), the normal filling effect coefficient (**b**), the enhanced filling effect coefficient (**c**), and the total effect coefficient (**d**) of hydrate-bearing quartz sands under different conditions of the initial hydrate saturation. The solid bule curve is drawn from Eq. (15) with different values of the fitting parameter m_1.

Table 1
The fitting parameters of Eq. (16) for the effective absolute permeability of hydrate-free and hydrate-bearing quartz sands under different conditions of the effective void ratio.

Initial hydrate saturation	The fitting parameters of Eq. (16)			R^2	Application range of the (effective) void ratio
	n_1	n_2	n_3		
0	66.7	−79.2	25.1	0.9895	[0.588, 0.710]
0.183	127	−108	23.8	0.9967	[0.424, 0.514]
0.351	265	−156	23.0	0.9991	[0.299, 0.369]
0.583	869	−289	23.6	0.9988	[0.160, 0.210]

When either coefficient exceeds unit, the positive effect of methane hydrate prevails. Fig. 15 displays N_E and N_K across the tested initial hydrate saturations. It is shown that N_E remains virtually unchanged with increasing initial hydrate saturation, whereas N_K rises slightly. Crucially, all values for both coefficients are well below unit, confirming that the negative influence of methane hydrate dominates the evolution of the effective void ratio and the effective absolute permeability.

4.4. Limitations and implications

A variety of theoretical and empirical expressions link soil hydraulic permeability to properties such as void ratio, specific surface area, and pore geometry; representative examples include the analytically derived Kozeny-Carman (KC) equation and empirical power- or exponential-form relations (Ren and Santamarina, 2018). For hydrate-bearing sediments, the KC equation is commonly taken as the starting framework for new models that correlate permeability with the hydrate saturation—defined as unit minus the ratio of effective porosity over intrinsic porosity (Dai and Seol, 2014; Lei et al., 2023; Liu et al., 2021). A semi-empirical extension of the KC equation has also been advanced to describe the hydraulic permeability of hydrate-bearing sediments under external loading (Zhang et al., 2022) and has since been adopted by other investigators (Xu et al., 2024). While these models capture the underlying physics, they offer limited precision in quantitative permeability predictions. To achieve a more accurate portrayal, this study proposes Eq. (16), a higher-order exponential form, whose coefficients of determination all exceeds 0.989 (Table 1). It must be emphasized that Eq. (16), with its specific parameter set, is valid only over the effective-void-ratio intervals specified in Table 1. The host-sediment void ratio in hydrate-bearing quartz sands spans 0.610–0.710, fully within the applicable range of 0.588–0.710; hence, Eq. (16) can be reliably applied to compute the host-sediment permeability. The same holds for the effective absolute permeability of hydrate-bearing sediments when compression-induced hydrate-saturation changes are disregarded. Although direct verification of this assumption is impractical—owing to measurement difficulties—the predicted values are regarded as optimal, and the

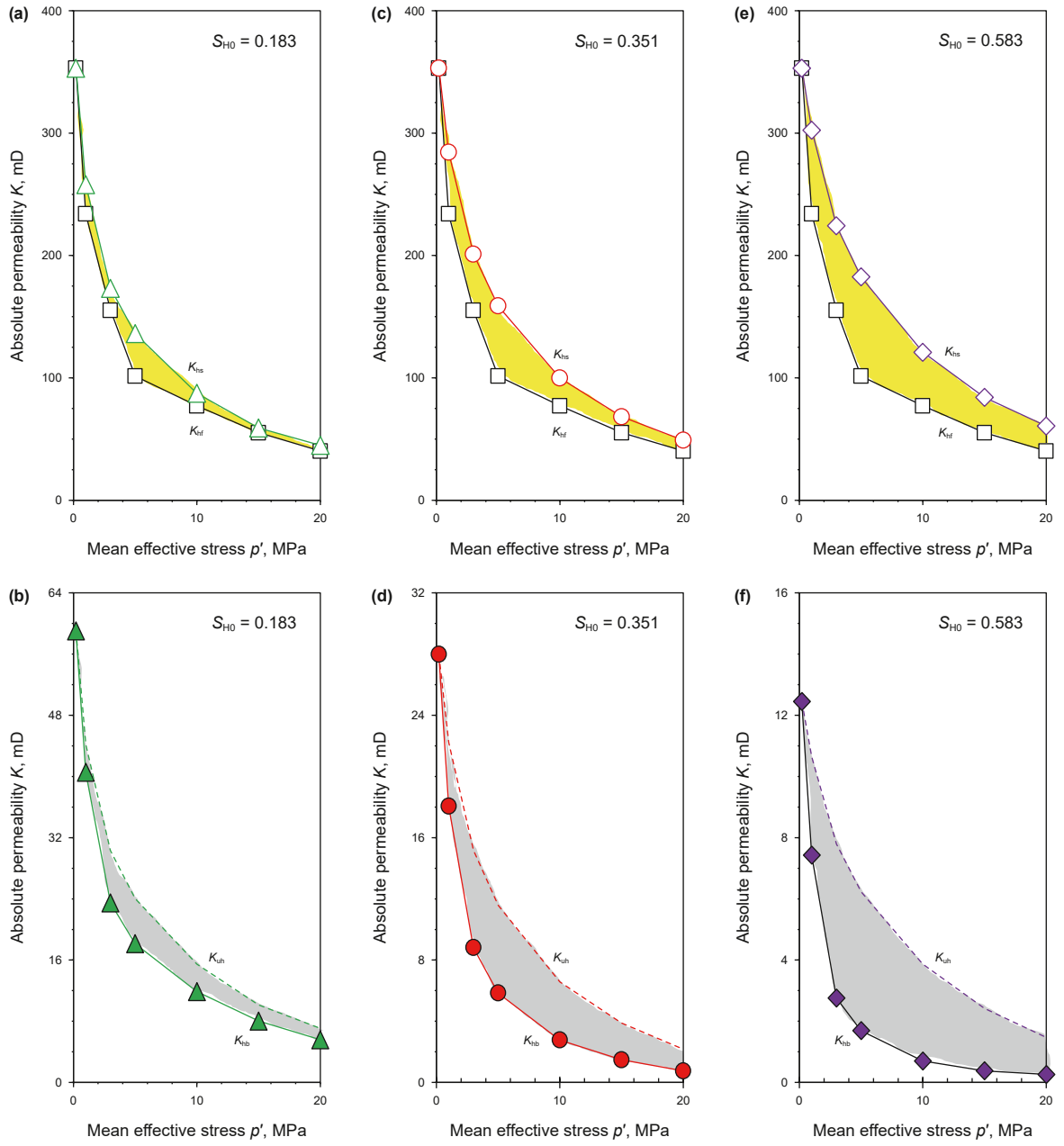

Fig. 13. Changes in the effective absolute permeability of hydrate-bearing quartz sands under isotropic loading. The initial hydrate saturation is 0.183 (**a**, **b**), 0.351 (**c**, **d**), and 0.583 (**e**, **f**). The open black squares in (a), (c), (e) represent the effective absolute permeability of hydrate-free sands. The open blue triangles in (a), red circles in (c), and purple diamonds in (e) stand for the effective absolute permeability of hydrate-bearing sands. The dashed curves with blue in (b), red in (d), and purple in (f) colors stand for the effective absolute permeability of hydrate-bearing sands without the hydrate saturation variation. The solid blue triangles in (b), red circles in (d), and purple diamonds in (f) represent the effective absolute permeability of hydrate-bearing sands with the hydrate saturation variation.

revealed physical bases for the positive and negative roles of methane hydrate remain trustworthy.

During depressurization-driven gas recovery from natural gas hydrates, the hydraulic permeability of the hydrate reservoir is governed by the structural characteristics of the fluid-occupied pore volume (Zhang et al., 2020); this volume, in turn, is jointly controlled by factors such as effective stress and hydrate saturation. Under external loading, higher hydrate saturation renders hydrate-bearing sediments less compressible (i.e., a larger host-sediment void ratio) yet simultaneously occupies more pore space. Consequently, an optimal hydrate saturation may exist that maximizes fluid-occupied pore volume while sustaining adequate hydraulic permeability. This study introduces a decoupling framework to quantify the positive and negative impacts of methane hydrate on both the effective void ratio and the effective absolute permeability, offering strong potential for optimizing hydraulic permeability during depressurization. However, the reported coefficients are strictly first-order estimates derived from a single monotonic loading-unloading cycle; they omit the hysteretic effects of cyclic stress reversals common near the wellbore. Multi-cycle loading could either further densify the skeleton—reducing permeability—or induce dilation and partially restore it. Consequently, direct upscaling of these coefficients to long-term production forecasts risks under- or over-predicting

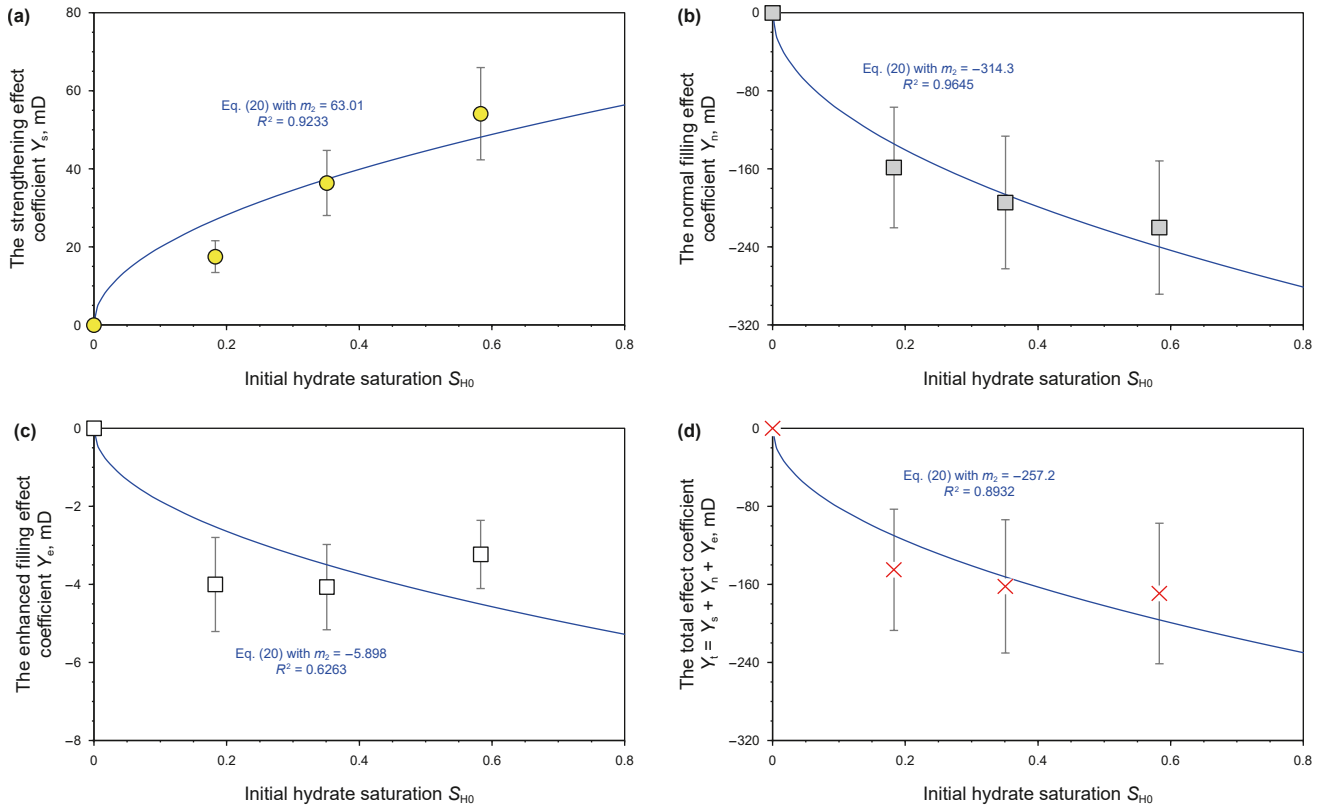

Fig. 14. With respect to the effective absolute permeability, changes in the strengthening effect coefficient (**a**), the normal filling effect coefficient (**b**), the enhanced filling effect coefficient (**c**), and the total effect coefficient (**d**) of hydrate-bearing quartz sands under different conditions of the initial hydrate saturation. The solid bule curve is drawn from Eq. (20) with different values of the fitting parameter m_2.

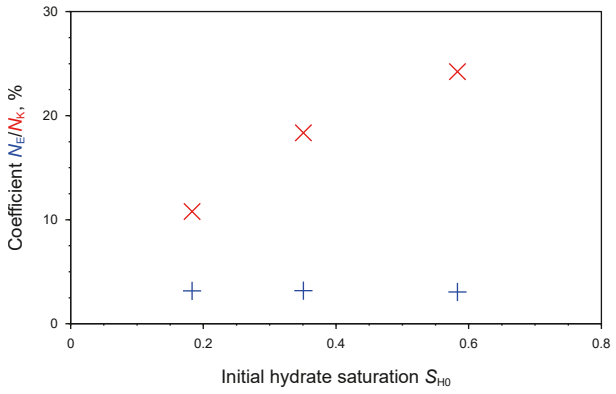

Fig. 15. Relative coefficient with respect to the effective void ratio N_E and the effective absolute permeability N_K of hydrate-bearing quartz sands subjected to isotropic loading under different conditions of the initial hydrate saturation. These two coefficients are calculated from Eqs. (21) and (22), providing in a percentage form.

injectivity and productivity, depending on the actual stress-path history.

By intentionally adopting an isothermal, drained framework, this study provides an essential baseline that cleanly isolates and quantifies the individual mechanical (stress-strain) and hydraulic (single-phase water flow) responses of hydrate-bearing sediments. This simplification eliminates the confounding effects of thermal and chemical processes, enabling—for the first time—a clear identification of the intrinsic links between hydrate saturation, effective stress, and permeability evolution. The resulting data set and constitutive relations therefore serve as a rigorous reference against which future fully coupled thermal-hydraulic-mechanical-chemical models can be benchmarked and calibrated, significantly reducing the uncertainty currently associated with multi-physics simulations of real hydrate production scenarios.

5. Conclusions

This study conducts isotropic compression/swelling and water-flow experiments on saturated hydrate-free and hydrate-bearing quartz sands, analyzing the intrinsic and effective void ratios together with the effective absolute permeability. A concise model is proposed to capture the evolution of the intrinsic void ratio in hydrate-bearing sands under isotropic loading and unloading. During loading, the positive and negative influences of methane hydrate on the effective void ratio and the effective absolute permeability are decoupled, quantified, and discussed. The principal findings are summarized below.

(1) The presence of methane hydrate in sand pores mitigates the decline in void ratio but amplifies the decrease in the effective void ratio under identical isotropic loading; residual changes in both void ratio and effective void ratio after unloading diminish with increasing hydrate saturation.
(2) The effective absolute permeability of hydrate-bearing sands declines with rising hydrate saturation and mean effective stress; hydrate occupancy restrains the cyclic-loading-induced damage to permeability. Permeability stress sensitivity weakens at higher mean effective stresses yet strengthens at higher hydrate saturations.

(3) Changes in the void ratio of hydrate-bearing sands during isotropic loading and unloading can be predicted with the compact model $e = e_0 - \alpha_p \ln\left(1 + \frac{p'}{P_r}\right)$ where $\frac{P_r(S_{H0})}{P_r(S_{H0}=0)} = 1 + d \cdot S_{H0}$, yielding a prediction error within ±1%. For loading, α_p equals the compression index $\lambda = 0.3685$; $P_r(S_{H0} = 0)$ equals 55.73 MPa, and $d = 1.264$ in this study. For unloading, α_p equals the swelling index $\kappa = 0.0178$ in this study; $P_r(S_{H0} = 0)$ equals 1.349 MPa which essentially invariant with hydrate saturation.

(4) Dedicated strengthening, normal filling, and the enhanced filling coefficients quantify the positive and negative impacts of methane hydrate on the effective void ratio and the effective absolute permeability. The absolute magnitudes of these coefficients grow with increasing initial hydrate saturation, and their normalized evolution obeys the simple expression $m\sqrt{S_{H0}}$. The normal filling coefficient exceeds the other two by one order of magnitude, confirming that hydrate filling governs the effective void-ratio and permeability responses of hydrate-bearing sands.

CRediT authorship contribution statement

Hui-Long Ma: Writing – original draft, Visualization, Methodology, Investigation, Formal analysis, Data curation. **Xiu-Li Feng:** Writing – review & editing, Validation, Supervision, Formal analysis. **Le-Le Liu:** Writing – review & editing, Writing – original draft, Visualization, Validation, Funding acquisition, Formal analysis, Conceptualization. **An Zhang:** Writing – review & editing, Validation, Methodology, Formal analysis. **Dong Wang:** Writing – review & editing, Supervision, Resources, Methodology, Funding acquisition, Conceptualization.

Data availability statement

The code used for data fitting is the Curve Fitting Toolbox in MATLAB R2022b, and the calculation is conducted in Excel Office (2019). Experimental and analytical data for plotting the graphs are available at https://doi.org/10.6084/m9.figshare.29422244.v1.

Declaration of interests

The authors declare that they have no known competing financial interests or personal relationships that could have appeared to influence the work reported in this paper.

Acknowledgements

This work has been jointly supported by the National Natural Science Foundation of China (Grant 42025702), the Natural Science Foundation of Shandong Province (Grant ZR2022YQ54), and the Taishan Scholars Program (No. tsqn202306297). All the support is immensely appreciated.

References

Alonso, E.E., Gens, A., Josa, A., 1990. A constitutive model for partially saturated soils. Geotechnique 40 (3), 405–430. https://doi.org/10.1680/geot.1990.40.3.405.

Cai, J.C., Xia, Y.X., Lu, C., Bian, H., Zou, S.M., 2020. Creeping microstructure and fractal permeability model of natural gas hydrate reservoir. Mar. Petrol. Geol. 115, 104282. https://doi.org/10.1016/j.marpetgeo.2020.104282.

Cao, L.X., Zhao, H., Yang, B.K., et al., 2024. A theoretical model for the hydraulic permeability of clayey sediments considering the impact of pore fluid chemistry. J. Mar. Sci. Eng. 12 (11), 1937. https://doi.org/10.3390/jmse12111937.

Cao, S.C., Li, X.L., Jung, J.W., Li, X.S., 2025. Experimental techniques for studying interfacial dynamics and sediment response during CH_4-CO_2 hydrate replacement. Capillarity 15 (3), 53–57. https://doi.org/10.46690/capi.2025.06.01.

Chang, Z.X., Zhou, C., 2025. A new model for water retention and hydraulic conductivity curves of deformable unsaturated soils. Water Resour. Res. 61 (5), e2024WR037826. https://doi.org/10.1029/2024WR037826.

Cheng, Q., Ng, C.W.W., Zhou, C., Tang, C.S., 2019. A new water retention model that considers pore non-uniformity and evolution of pore size distribution. Bull. Eng. Geol. Environ. 78 (7), 5055–5065. https://doi.org/10.1007/s10064-019-01476-4.

Chong, Z.R., Yang, S.H.B., Babu, P., Linga, P., Li, X.S., 2016. Review of natural gas hydrates as an energy resource: prospects and challenges. Appl. Energy 162, 1633–1652. https://doi.org/10.1016/j.apenergy.2014.12.061.

Cui, L.Y., Zhou, C., Liu, L.L., 2025. Water retention model for hydrate-bearing sediments considering pore structure evolution. Can. Geotech. J. https://doi.org/10.1139/cgj-2025-0417.

Dai, S., Lee, C., Santamarina, J.C., 2011. Formation history and physical properties of sediments from the Mount Elbert Gas hydrate stratigraphic test Well, Alaska North Slope. Mar. Petrol. Geol. 28 (2), 427–438. https://doi.org/10.1016/j.marpetgeo.2010.03.005.

Dai, S., Santamarina, J.C., Waite, W.F., Kneafsey, T.J., 2012. Hydrate morphology: physical properties of sands with patchy hydrate saturation. J. Geophys. Res. Solid Earth 117 (B11). https://doi.org/10.1029/2012JB009667.

Dai, S., Seol, Y., 2014. Water permeability in hydrate-bearing sediments: a pore-scale study. Geophys. Res. Lett. 41 (12), 4176–4184. https://doi.org/10.1002/2014gl060535.

Delli, M.L., Grozic, J.L.H., 2014. Experimental determination of permeability of porous media in the presence of gas hydrates. J. Pet. Sci. Eng. 120, 1–9. https://doi.org/10.1016/j.petrol.2014.05.011.

Fang, Y., Flemings, P.B., Germaine, J.T., et al., 2022. Compression behavior of hydrate-bearing sediments. AAPG Bull. 106 (5), 1101–1126. https://doi.org/10.1306/01132221002.

Gong, B., Lei, G., Chen, L., Zhao, Y., 2025. Mitigating risks in deep sea gas hydrate production: A new perspective on interpreting thermo-hydro-mechanical feedbacks. Adv. Geo-Energy Res. 17 (3), 267–270. https://doi.org/10.46690/ager.2025.09.08.

Huang, L., Su, Z., Wu, N.Y., Cheng, J.W., 2016. Analysis on geologic conditions affecting the performance of gas production from hydrate deposits. Mar. Petrol. Geol. 77, 19–29. https://doi.org/10.1016/j.marpetgeo.2016.05.034.

Hyodo, M., Yoneda, J., Yoshimoto, N., Nakata, Y., 2013. Mechanical and dissociation properties of methane hydrate-bearing sand in deep seabed. Soils Found. 53 (2), 299–314. https://doi.org/10.1016/j.sandf.2013.02.010.

Jang, J., Cao, S.C., Stern, L.A., Jung, J., Waite, W.F., 2018. Impact of pore fluid chemistry on fine-grained sediment fabric and compressibility. J. Geophys. Res. Solid Earth 123 (7), 5495–5514. https://doi.org/10.1029/2018jb015872.

Khan, S., Khulief, Y., Juanes, R., et al., 2024. Geomechanical modeling of CO_2 sequestration: a review focused on CO_2 injection and monitoring. J. Environ. Chem. Eng. 12 (3), 112847. https://doi.org/10.1016/j.jece.2024.112847.

Kim, A.R., Kim, J.T., Cho, G.C., Lee, J.Y., 2018. Methane production from marine gas hydrate deposits in Korea: thermal-hydraulic-mechanical simulation on production wellbore stability. J. Geophys. Res. Solid Earth 123 (11), 9555–9569. https://doi.org/10.1029/2018jb015875.

Kumar, A., Maini, B., Bishnoi, P.R., et al., 2010. Experimental determination of permeability in the presence of hydrates and its effect on the dissociation characteristics of gas hydrates in porous media. J. Pet. Sci. Eng. 70 (1), 114–122. https://doi.org/10.1016/j.petrol.2009.10.005.

Lee, J.Y., Santamarina, J.C., Ruppel, C., 2010. Volume change associated with formation and dissociation of hydrate in sediment. Geochem. Geophys. Geosyst. 11 (3). https://doi.org/10.1029/2009GC002667.

Lei, G., Gong, Z.C., He, Z.J., et al., 2023. Theoretical analysis of shape factor of gas hydrate sediments under stress dependence. Gas Sci. Eng. 119, 205137. https://doi.org/10.1016/j.jgsce.2023.205137.

Lei, L., Seol, Y., 2020. Pore-scale investigation of methane hydrate-bearing sediments under triaxial condition. Geophys. Res. Lett. 47 (5), e2019GL086448. https://doi.org/10.1029/2019GL086448.

Li, G.Y., Ding, Y.L., Zhang, H.T., Dai, S., 2025. Impacts of particle size distribution on the permeability of hydrate-bearing sediments using a DEM-PNM approach. Comput. Geotech. 184, 107314. https://doi.org/10.1016/j.compgeo.2025.107314.

Li, J.F., Ye, J.L., Qin, X.W., et al., 2018. The first offshore natural gas hydrate production test in South China Sea. China Geol. 1 (1), 5–16. https://doi.org/10.31035/cg2018003.

Li, Y.B., Xu, T.F., Xin, X., et al., 2024. Multi-scale comprehensive study of the dynamic evolution of permeability during hydrate dissociation in clayey silt hydrate-bearing sediments. Adv. Geo-Energy Res. 12 (2), 127–140. https://doi.org/10.46690/ager.2024.05.05.

Liu, L.L., Lu, X.B., Zhang, X.H., 2015. A theoretical model for predicting the spatial distribution of gas hydrate dissociation under the combination of depressurization and heating without the discontinuous interface assumption. J. Pet. Sci. Eng. 133, 589–601. https://doi.org/10.1016/j.petrol.2015.07.005.

Liu, L.L., Sun, Q.C., Wu, N.Y., et al., 2021. Fractal analyses of the shape factor in Kozeny-Carman equation for hydraulic permeability in hydrate-bearing sediments. Fractals 29 (7), 2150217. https://doi.org/10.1142/S0218348x21502170.

Liu, L.L., Zhang, Z., Li, C.F., et al., 2020. Hydrate growth in quartzitic sands and implication of pore fractal characteristics to hydraulic, mechanical, and

electrical properties of hydrate-bearing sediments. J. Nat. Gas Sci. Eng. 75, 103109. https://doi.org/10.1016/j.jngse.2019.103109.
Luo, T.T., Li, Y.H., Madhusudhan, B.N., Zhao, J.F., Song, Y.C., 2020. Comparative analysis of the consolidation and shear behaviors of CH_4 and CO_2 hydrate-bearing silty sediments. J. Nat. Gas Sci. Eng. 75, 103157. https://doi.org/10.1016/j.jngse.2020.103157.
Myshakin, E.M., Seol, Y., Lin, J.S., et al., 2019. Numerical simulations of depressurization-induced gas production from an interbedded turbidite gas hydrate-bearing sedimentary section in the offshore India: site NGHP-02-16 (Area-B). Mar. Petrol. Geol. 108, 619–638. https://doi.org/10.1016/j.marpetgeo.2018.10.047.
Nakashima, K., Nakata, Y., Hyodo, M., et al., 2021. Compressive characteristics of methane hydrate-bearing sands under isotropic consolidation. Soils Found. 61 (2), 506–519. https://doi.org/10.1016/j.sandf.2021.01.011.
Ouchi, H., Yamamoto, K., Akamine, K., et al., 2022. Numerical history-matching of modeling and actual gas production behavior and causes of the discrepancy of the Nankai Trough gas-hydrate production test cases. Energy Fuels 36 (1), 210–226. https://doi.org/10.1021/acs.energyfuels.1c02931.
Ren, X.W., Santamarina, J.C., 2018. The hydraulic conductivity of sediments: a pore size perspective. Eng. Geol. 233, 48–54. https://doi.org/10.1016/j.enggeo.2017.11.022.
Sawyer, D.E., DeVore, J.R., 2015. Elevated shear strength of sediments on active margins: evidence for seismic strengthening. Geophys. Res. Lett. 42 (23), 10216–10221. https://doi.org/10.1002/2015gl066603.
Sloan, E.J.r., 2003. Fundamental principles and applications of natural gas hydrates. Nature 426 (6964), 353–359. https://doi.org/10.1038/nature02135.
Stoecklin, A., Friedli, B., Puzrin, A.M., 2017. Sedimentation as a control for large submarine landslides: mechanical modeling and analysis of the Santa Barbara Basin. J. Geophys. Res. Solid Earth 122 (11), 8645–8663. https://doi.org/10.1002/2017jb014752.
Sun, P., Lu, H., Yang, J., et al., 2022. Numerical study on shear interaction between the track plate of deep-sea mining vehicle and the seafloor sediment based on CEL method. Ocean Eng. 266, 112785. https://doi.org/10.1016/j.oceaneng.2022.112785.
Suzuki, K., Ebinuma, T., Narita, H., 2009. Features of methane hydrate-bearing sandy-sediments of the Forearc Basin along the Nankai Trough: effect on methane hydrate-accumulating mechanism in turbidite. Chigaku Zasshi 118, 899–912. https://doi.org/10.5026/jgeography.118.899.
Tian, H.T., Liu, W.H., Ding, P.B., et al., 2024. Numerical simulation of elastic properties of hydrate-bearing sediments with digital rock technology. Mar. Petrol. Geol. 160, 106592. https://doi.org/10.1016/j.marpetgeo.2023.106592.
Uchida, S., Soga, K., Yamamoto, K., 2012. Critical state soil constitutive model for methane hydrate soil. J. Geophys. Res. Solid Earth 117 (B3). https://doi.org/10.1029/2011JB008661.
Wan, Y.Z., Wu, N.Y., Chen, Q., et al., 2022. Coupled thermal-hydrodynamic-mechanical-chemical numerical simulation for gas production from hydrate-bearing sediments based on hybrid finite volume and finite element method. Comput. Geotech. 145, 104692. https://doi.org/10.1016/j.compgeo.2022.104692.
Wang, H.J., Liu, W.G., Sun, X., Pan, X.L., Li, Y.H., 2021. Experimental study on the gas permeability of marine sediments with various hydrate saturations and effective stresses. Energy Fuels 35 (21), 17479–17489. https://doi.org/10.1021/acs.energyfuels.1c02465.
Xia, Y.X., Elsworth, D., Xu, S., et al., 2025. Pore-scale gas-water two-phase flow and relative permeability characteristics of disassociated hydrate reservoir. Pet. Sci. 22 (8), 3344–3356. https://doi.org/10.1016/j.petsci.2025.04.030.
Xu, J.L., Huang, Z.Y., Xu, C.S., Zhang, J.H., Wang, R., 2024. Experimental investigation on methane hydrate-bearing sediment permeability under a wide range of conditions. Appl. Ocean Res. 150, 104095. https://doi.org/10.1016/j.apor.2024.104095.
Xu, J.L., Xu, C.S., Yoshimoto, N., et al., 2022. Compression and deformation characteristics of hydrate-bearing sediments under high effective confining pressure. Int. J. Geomech. 22 (6), 04022067. https://doi.org/10.1061/(ASCE)GM.1943-5622.0002382.
Yamamoto, K., Wang, X.X., Tamaki, M., Suzuki, K., 2019. The second offshore production of methane hydrate in the Nankai Trough and gas production behavior from a heterogeneous methane hydrate reservoir. RSC Adv. 9 (45), 25987–26013. https://doi.org/10.1039/c9ra00755e.
Yan, R.T., Yu, H.F., Yang, D.H., Wu, Y.C., Tang, H., 2023. Isotropic compression behavior for methane hydrate-bearing soil with varying temperature and pore pressure. Int. J. Hydrogen Energy 48 (93), 36327–36339. https://doi.org/10.1016/j.ijhydene.2023.06.046.
Yang, D.H., Yan, R.T., Yan, M.Q., Lu, D., Wei, C.F., 2023. Geomechanical properties of artificial methane hydrate-bearing fine-grained sediments. Gas Sci. Eng. 109, 104852. https://doi.org/10.1016/j.jngse.2022.104852.
Ye, J.L., Qin, X.W., Xie, W.W., et al., 2020. The second natural gas hydrate production test in the South China Sea. China Geol 3 (2), 197–209. https://doi.org/10.31035/cg2020043.
Yoneda, J., Masui, A., Konno, Y., et al., 2015. Mechanical properties of hydrate-bearing turbidite reservoir in the first gas production test site of the Eastern Nankai Trough. Mar. Petrol. Geol. 66, 471–486. https://doi.org/10.1016/j.marpetgeo.2015.02.029.
Zhang, A., Jiang, M.J., Wang, D., Li, Q.P., 2023a. Three-dimensional DEM investigation of mechanical behaviors of grain-cementing type methane hydrate-bearing sediment. Acta Geotech 18 (12), 6371–6394. https://doi.org/10.1007/s11440-023-01903-7.
Zhang, N., Zhai, W.K., Yin, S.Y., et al., 2025a. Deep-sea soft soil and deep-sea mining vehicle interaction: from soil properties to locomotion performance. Appl. Ocean Res. 154, 104372. https://doi.org/10.1016/j.apor.2024.104372.
Zhang, Y.C., Liu, L.L., Luo, L., et al., 2025b. Permeability prediction in hydrate-bearing sediments via pore network modeling. Adv. Geo-Energy Res. 16 (2), 158–170. https://doi.org/10.46690/ager.2025.05.07.
Zhang, Z., Li, C.F., Ning, F.L., et al., 2020. Pore fractal characteristics of hydrate-bearing sands and implications to the saturated water permeability. J. Geophys. Res. Solid Earth 125 (3), e2019JB018721. https://doi.org/10.1029/2019JB018721.
Zhang, Z., Liu, L.L., Lu, W.J., et al., 2023b. Permeability of hydrate-bearing fine-grained sediments: research status, challenges and perspectives. Earth-Sci. Rev. 244, 104517. https://doi.org/10.1016/j.earscirev.2023.104517.
Zhang, Z., Liu, L.L., Ning, F.L., et al., 2022. Effect of stress on permeability of clay silty cores recovered from the Shenhu hydrate area of the South China Sea. J. Nat. Gas Sci. Eng. 99, 104421. https://doi.org/10.1016/j.jngse.2022.104421.
Zhao, J.Z., Zheng, J.C., Ren, L., Lin, R., Zhou, B., 2024. A review on geological storage of marine carbon dioxide: challenges and prospects. Mar. Petrol. Geol. 163, 106757. https://doi.org/10.1016/j.marpetgeo.2024.106757.
Zhao, Y.P., Hu, G.W., Liu, L.L., et al., 2025. Mechanical properties of gas hydrate-bearing sediments: research progress, challenges and perspectives. Earth-Sci. Rev. 262, 105058. https://doi.org/10.1016/j.earscirev.2025.105058.
Zhao, Y.P., Liu, J.Q., Sang, S.K., et al., 2023. Experimental investigation on the permeability characteristics of methane hydrate-bearing clayey-silty sediments considering various factors. Energy 269, 126811. https://doi.org/10.1016/j.energy.2023.126811.
Zhou, C., Ng, C.W.W., 2014. A new and simple stress-dependent water retention model for unsaturated soil. Comput. Geotech. 62, 216–222. https://doi.org/10.1016/j.compgeo.2014.07.012.
Zhou, J.Z., Yang, Z.J., Wei, C.F., Chen, P., Yan, R.T., 2021. Mechanical behavior of hydrate-bearing sands with fine particles under isotropic and triaxial compression. J. Nat. Gas Sci. Eng. 92, 103991. https://doi.org/10.1016/j.jngse.2021.103991.
Zhou, M.L., Soga, K., Yamamoto, K., 2020a. Upscaling techniques for fully coupled THM simulation and application to hydrate gas production tests. Comput. Geotech. 124, 103596. https://doi.org/10.1016/j.compgeo.2020.103596.
Zhou, M.L., Soga, K., Yamamoto, K., Huang, H.W., 2020b. Geomechanical responses during depressurization of hydrate-bearing sediment formation over a long methane gas production period. Geomech. Energy Environ. 23, 100111. https://doi.org/10.1016/j.gete.2018.12.002.
Zulberti, A., Jones, N.L., Ivey, G.N., 2020. Observations of enhanced sediment transport by nonlinear internal waves. Geophys. Res. Lett. 47 (19), e2020GL088499. https://doi.org/10.1029/2020GL088499.